RESEARCH ARTICLE



Infrasound observations and constraints on the 2018 eruption of Kīlauea Volcano, Hawaii

Weston Thelen¹ • Gregory Waite² • John Lyons³ • David Fee⁴

Received: 30 September 2021 / Accepted: 24 June 2022 This is a U.S. Government work and not under copyright protection in the US; foreign copyright protection may apply 2022

Abstract

The 2018 eruption of Kīlauea Volcano was a dynamic event involving explosions, collapses, and fountaining at multiple vents spread over tens of kilometers. The permanent infrasound network operated by the USGS Hawaiian Volcano Observatory (HVO) was well prepared to observe the collapse of the summit, and additional deployments permitted infrasound observations during fissuring in the lower East Rift Zone (LERZ). We provide a summary of infrasound observations, including lava lake spattering, collapses, explosions, rockfall, and lava fountaining, using seismicity and tilt at times to help constrain our interpretations. At the summit of Kīlauea Volcano, we document the process of partial caldera collapse and examine a set of "proto-collapse" events that precede the widely observed events but share many of the same qualities as the larger collapses. For the initial twelve collapse events, we compare the timing of collapse onset to other observations and illustrate the repeatable characteristics of the recorded waveforms and infrasound characteristics associated with each episode of caldera collapse. In the LERZ, we match the acoustic signals with visual observations, including fissure migration, explosions near fissures, and littoral explosions. Lastly, we document and discuss the performance of infrasound alarms during the 2018 Kīlauea eruption. In general, alarming became successful in detecting collapse events at the summit of the volcano after tuning and became a key discriminant in the initial determination of collapse events, especially when visual observations were not available.

Keywords Infrasound · Fountaining · Littoral explosion · Explosion · Caldera collapse · Kīlauea Volcano

Introduction

Kīlauea Volcano, Hawai'i, is a basaltic, shield-style volcano with linear rift zones extending many tens of kilometers from a topographically high summit caldera (Tilling and

This paper constitutes part of a topical collection:

The historic events at Kilauea Volcano in 2018: summit collapse, rift zone eruption, and Mw6.9 earthquake

Editorial responsibility: A. Harris

Published online: 19 July 2022

- Weston Thelen wthelen@usgs.gov
- USGS Cascades Volcano Observatory, Vancouver, WA, USA
- ² Michigan Technological University, Houghton, MI, USA
- ³ USGS Alaska Volcano Observatory, Anchorage, AK, USA
- Alaska Volcano Observatory and Wilson Alaska Technical Center, Geophysical Institute, University of Alaska Fairbanks, Fairbanks, AK, USA

Dvorak 1993). Between 1983 and 2018, Kīlauea Volcano erupted from areas at or near Pu'u'ō'ō along its East Rift Zone in a nearly continuous manner (e.g., Wolfe et al. 1987; Heliker and Mattox 2003; Wright and Klein 2014). Between 2008 and 2018, Kīlauea Volcano also erupted from within the summit caldera of the volcano, where a lava lake formed producing minor overflows onto the surrounding crater floor (Fig. 1; Patrick et al. 2021). Early on May 1, 2018 (UTC), a down-rift dike intrusion and collapse of Pu'u'ō'ō lava shield marked the beginning of a change in activity at Kīlauea, where magma that erupted in the lower East Rift Zone (LERZ) near Leilani Estates drained the shallow magmatic system at the summit of the volcano (Neal et al. 2019). This draining resulted in a cycle of collapse events within the summit caldera of the volcano and voluminous extrusion of lava flows into communities of southeast Hawai'i Island (Neal et al. 2019). We review the infrasound records for the collapse, explosive, fountaining, and fissure opening event associated with this eruptive phase, thereby providing a library for future use wherever such events take place (cf. Piton de la Fournaise 2007, Staudacher et al. 2009).



76 Page 2 of 24 Bulletin of Volcanology (2022) 84:76

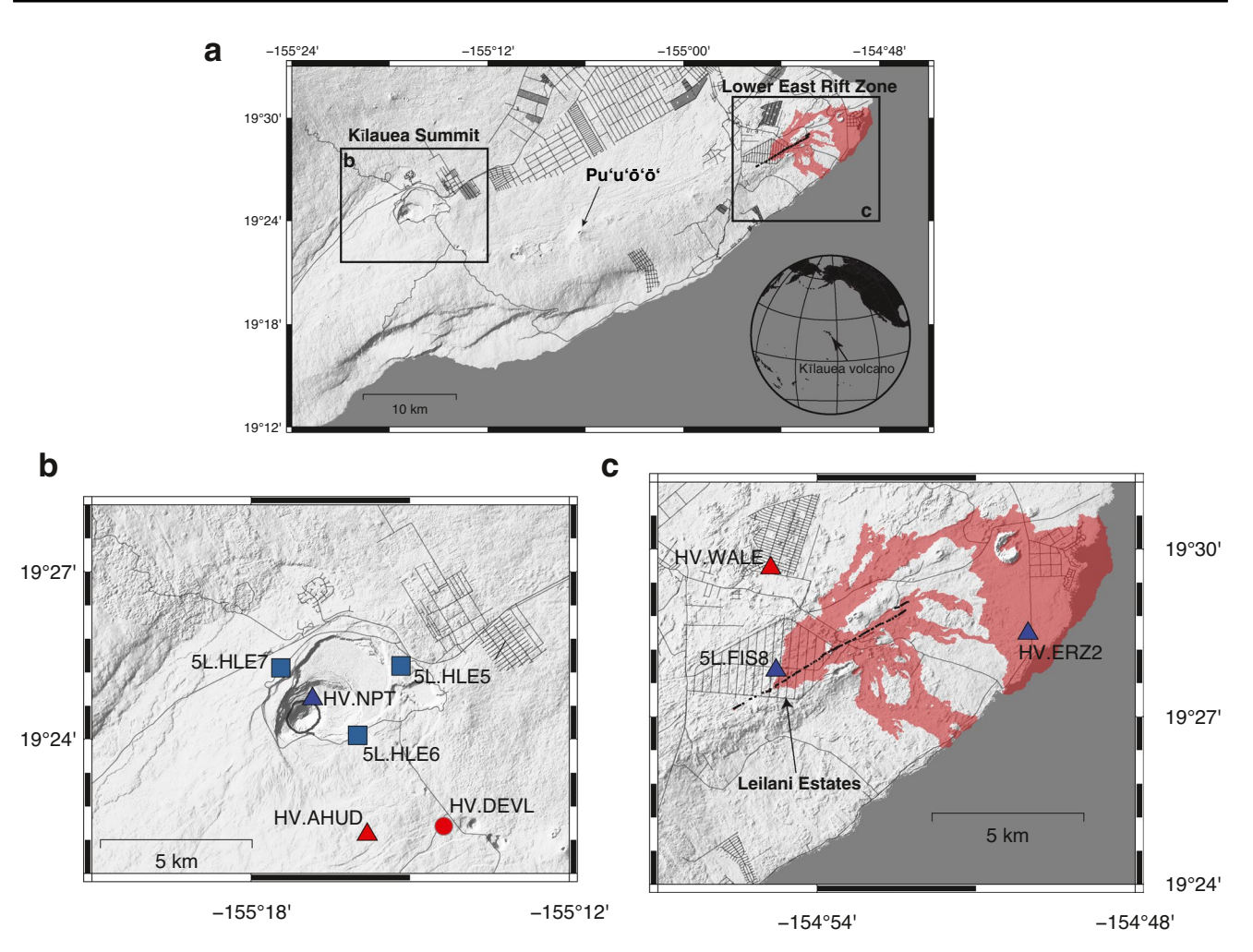


Fig. 1 Location map overview (a), Kīlauea summit (b), and lower East Rift Zone (c). Maps of infrasound arrays and single-site locations. Red triangles show permanent array sites; blue triangles show arrays installed in response to unrest. Red circles show seismic-only stations mentioned in this paper (AHUD and NPT also have seismometers). Blue squares show single infrasound sensors. Gray circle

in **b** shows the original outline of the Halema'uma'u crater. Black solid lines in **c** show fissure locations, and red colored areas shown lava inundation from the 2018 eruption. Stations are labeled first by their network code, then station code separated by a period. Figure generated with GMT (Wessel et al. 2019)

Infrasound refers to sound waves traveling in the atmosphere at frequencies below the human perception of hearing (≤20 Hz). Volcanoes commonly produce infrasound from a variety of processes, including explosions, rockfall, spattering, and any other process that moves air turbulently (e.g., Fee et al. 2011; Johnson and Ripepe 2011; De Angelis et al. 2019). Infrasound at local scales travels relatively free of attenuation, compared to seismic waves, and wind is the main source of noise in the infrasound band (Bowman et al. 2005). Ideal infrasound installations can thus be positioned farther from the source, often in forest or heavy brush that can dampen wind noise. Infrasound instruments are also often deployed in arrays or groups of three or more instruments placed in a strategic configuration (e.g., Johnson and Ripepe 2011; Fee et al. 2011; De Angelis et al. 2019). The arrangement of instruments enables assessment of the direction of an incoming signal based on time differences between instruments (e.g., Rost and Thomas 2002; Ripepe and Marchetti 2002; Olson and Szuberla 2005; Haney et al. 2018; De Angelis et al. 2019).

Infrasound has a long and rich history of observation on Kīlauea Volcano made possible by frequent eruptions. As early as the mid-twentieth century, acoustic measurements were made at Kīlauea (Perret 1950). More recently, the nearly continuous eruption from the area at and around Puʻuʻōʻō, and eventually the summit eruption that began in 2008, prompted studies by Garces et al. (2003) and Matoza et al. (2010), who used infrasound arrays to study continuous infrasonic tremor emanating from Puʻuʻōʻō and intermittently from lava tube skylights. Fee and Garcés (2007) noted clear diurnal variations in infrasonic tremor from Puʻuʻōʻō and related it to changes in the atmospheric boundary layer.



Bulletin of Volcanology (2022) 84:76 Page 3 of 24 76

Fee et al. (2010) studied signals coming from the summit vent in 2008 and early 2009. They observed broadband infrasonic transients associated with degassing bursts and continuous tremor associated with persistent degassing. Fee et al. (2011) detected the collapse of Pu'u'ō'ō crater in 2007 and tracked the subsequent fissure eruption in the East Rift Zone. Patrick et al. (2011, 2016) used infrasound as part of a multi-disciplinary study to understand the trigger for very-long-period earthquakes and gas pistoning. Marcillo and Johnson (2010) looked at atmospheric conditions near Kīlauea using infrasound. Finally, Thelen and Cooper (2014) also explored the infrasound at the summit of Kīlauea arising from rockfall and degassing fluctuations in the summit lava lake. These studies informed our interpretations of signals observed during the 2018 eruption of Kīlauea Volcano.

In this paper, we summarize the available infrasound data and discuss many of the interesting features of the 2018 eruption. The infrasound network during the eruption was dynamic due to equipment losses from volcanic activity and additions to keep up with the changing eruption conditions. Campaign-style infrasound was deployed at both the summit and LERZ and provided complementary but shorter-time period infrasound observations (e.g., Patrick et al. 2019a, b; Lyons et al. 2021). This discussion is observational and descriptive with only limited analysis due to the summary nature of the paper. We largely treat the summit eruption and the LERZ eruption separately, as the USGS Hawaiian Volcano Observatory (HVO) did during the response, because it helps focus the discussion on a subset of processes that are unique to each location. We encourage deeper, more detailed study and hope that this paper facilitates that work. Lastly, we discuss the valuable role of infrasound within the operational environment of the eruption.

Data and methods

HVO is responsible for monitoring Kīlauea Volcano and does so with a variety of instrumentation operated by HVO and its partners (USGS HVO 1956). At the beginning of 2018, the permanent infrasound network around the Island of Hawai'i consisted of three arrays around the summit of Kīlauea (stations AHUD, MENE and AIND) and another array on the west flank of Hualalai (KHLU), operated by the University of Hawai'i at Manoa (Fig. 1; Garcés and Thelen 2015). In addition to the permanent arrays, there was a temporary real-time array installed just north of the Halema'uma'u crater (NPT). At the beginning of the 2018 eruption, only NPT and AHUD were fully operational and providing real-time data. Three additional single infrasound sites were installed around the summit of Kīlauea in late May 2018 and recorded on site (see supplementary material). After the eruption started in the lower East Rift Zone (LERZ), additional real-time infrasound arrays (ERZ2 and WALE) were installed to track changes in vent location. Another array (FIS8) was installed close to fissure 8 in June and recorded on site as well (Lyons et al. 2021). Relevant parameters for the arrays used in this paper can be found in Supplementary Table 1 and Supplementary Fig. 1.

Infrasound sensors at sites AHUD and ERZ2 were VDP-10 sensors, detailed in Thelen and Cooper (2014). The NPT array used infraBSU sensors (Marcillo et al. 2012), and the WALE array used Chaparral M60 sensors. Overall gains, including the digitizer and sensor, can be found in Supplementary Table 1. The combined response of the sensor and digitizer can be assumed to be flat between approximately 80 s and the Nyquist frequency for stations AHUD, ERZ2, and WALE, and approximately 20 s and the Nyquist frequency for station NPT. Details of the response of different stages can be found at the Incorporated Research Institutions for Seismology (IRIS) archive.

Infrasound monitoring involves locating and characterizing the size and nature of the source. While there are many techniques that can be used to analyze infrasound data, we leveraged array processing techniques to characterize the 2018 eruption sequence. One of the most basic calculations for an array is the estimation of a slowness vector from the passage of a coherent wave across the individual array elements. The slowness vector is often further reduced to a back-azimuth and apparent velocity. Here we use least squares beamforming to obtain these parameters (Olson and Szuberla 2005; Bishop et al. 2020). We use the mean of the peak cross-correlation coefficient between elements (MCCM) and the apparent velocity to evaluate the quality of the calculated back-azimuth. In general, we use 30-s windows with 50% overlap to estimate the back-azimuth. These parameters mimic the properties used in real-time processing at HVO and reduce the effects of window edges cutting off transients. Additional details can be found in Haney et al. (2018) and Bishop et al. (2020). At times, we use the calculated slowness and back-azimuth, or assume a slowness and back-azimuth, to then shift and stack the individual elements into a single trace called delay and sum beamforming (Rost and Thomas 2002). We also employ the infrasound parameter (IP), which is a product of the number of detections in an azimuthal range and the amplitude of the signal over a given duration (Ulivieri and Marchetti 2013). The infrasound analysis, including many of the libraries used in this paper, relies heavily on the Obspy library (Beyreuther et al. 2010).

In addition to the infrasound network, Kīlauea is monitored with a dense network of seismometers, Global Navigation Satellite System (GNSS) receivers, and tiltmeters around the summit of the volcano, and a sparser network of seismometers and GNSS receivers in the LERZ around Leilani Estates (Fig. 1; Johanson and Miklius 2019; Shiro et al. 2021). The combined observations of this multiparametric network make the 2018 eruption at Kīlauea provides

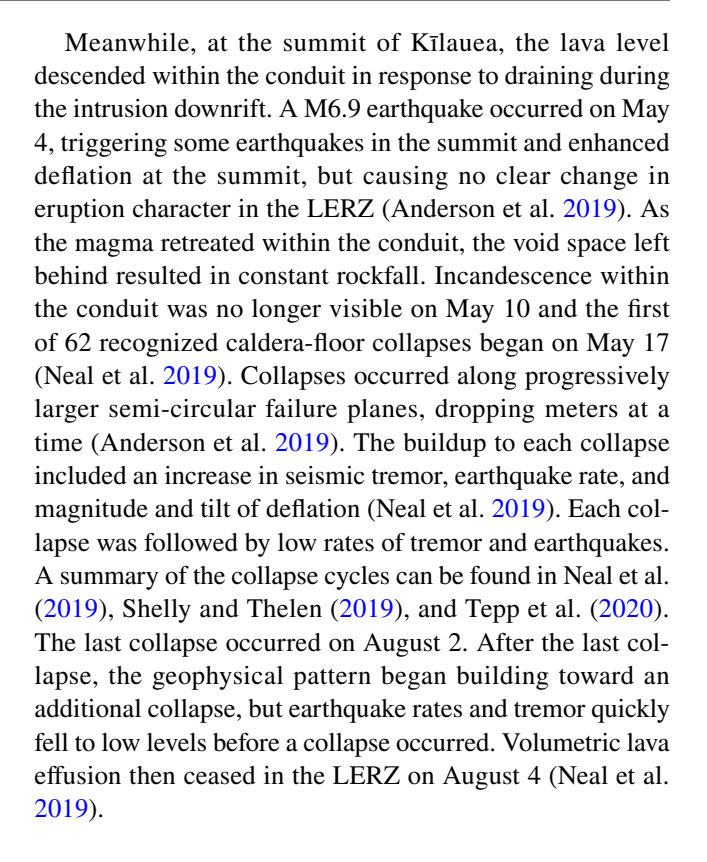


an excellent example of caldera collapse, Hawaiian-style lava fountaining, and fissure eruptions.

Activity overview

Here, we summarize the overall activity to provide some perspective of eruptive activity before discussing the details of each eruption location. In early 2018, two eruptions had been occurring at Kīlauea, the Pu'u'ō'ō eruption in the middle East Rift Zone and the summit eruption within Halema'uma'u crater (Patrick et al. 2021). Magma beneath Kīlauea actually transited both eruption sites, starting in storage regions under the summit, degassing at shallow levels within the summit lava lake and conduit, and then traveling down the East Rift Zone to Pu'u'ō'ō, where it was emplaced as lava flows (e.g., Garcia et al. 1992; Ryan 1988; Poland et al. 2014).

Activity began escalating in early 2018, when the rate of lava issuing from Pu'u'ō'ō, the dominant vent since 1983, slowed, creating an imbalance of magma flux in the rift zone and a rising lava lake level at the summit (Fig. 1; Neal et al. 2019; Patrick et al. 2019). The additional pressurization caused earthquakes and inflation in the summit area and earthquakes in the upper East Rift Zone connector, a common phenomenon in unrest at Kīlauea (Klein et al. 1987). The pattern of unrest was similar to many prior episodes during the Pu'u'ō'ō eruption (e.g., Episodes 59, 60, 61; Patrick et al. 2019a, b). As the backup continued, the lava lake level rose until the lava lake began overflowing onto the Halema'uma'u crater floor in late April. High lava lake levels and overflows were not unprecedented during the 2008-2018 summit eruption and often resulted in intrusions or new eruptive episodes in the East Rift Zone. Late on April 30 local time (May 1 UTC), after a brief breakout of lava on the west side of the Pu'u'ō'ō cone, an intrusion started from the vicinity of Pu'u'ō'ō and traveled downrift (Neal et al. 2019; Patrick et al. 2021; Poland et al. 2021a, b). After approximately 36 h of downrift travel, the intrusion stalled beneath the Leilani Estates subdivision in the lower East Rift Zone (LERZ). On May 3 at approximately 17:00 local time (May 4 3:00 UTC), the first of 24 fissures began erupting (Neal et al. 2019). Low flux fissures continued, effusing mostly stored magmas, until fresh hot magma from the summit arrived in the LERZ in late May producing more voluminous lava flows, first traveling south to the ocean, then consolidating at fissure 8 (later named Ahu'ailā'au) where it remained until the eruption's end (Fig. 6; Neal et al. 2019; Gansecki et al. 2019). In this paper, we refer to the eruptive vent as fissure 8, as was done during the eruption response, and we refer to Ahu'ailā'au as the cone that is a result of the eruption.



Summit infrasound

Below we describe features of the infrasound observed as part of the lava lake and summit caldera collapse. We start with a description of events including gas piston events, composite events, emission events, collapses, and protocollapses. Then, we describe the overall chronology of the events and discuss what processes may be responsible for the observations.

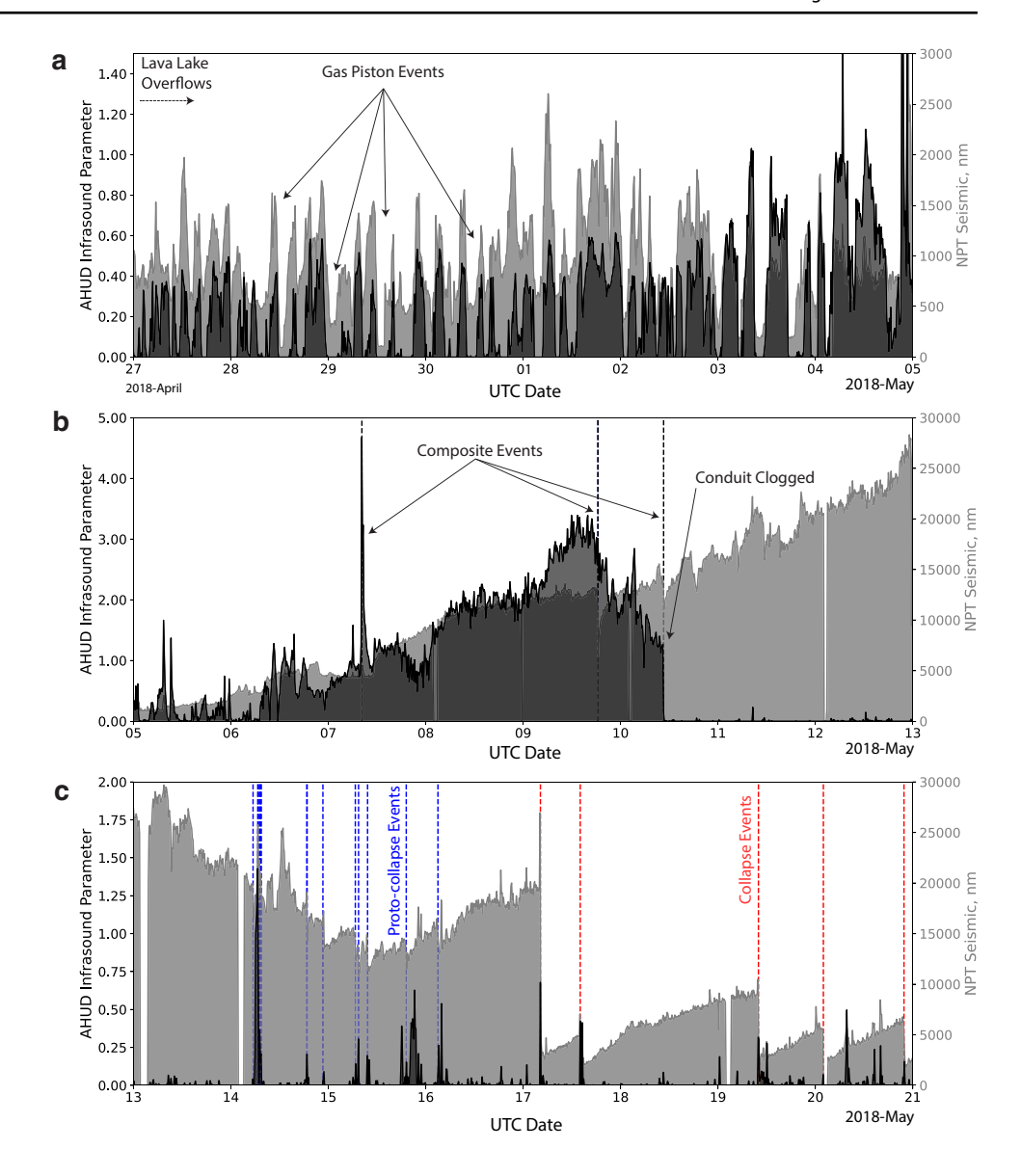
Gas piston events

Gas piston cycles were common during the 2008–2018 summit eruption (Fig. 2). Once the lava lake was fully established, fluctuations in degassing (spattering) were closely tied to the amplitude of seismic and infrasonic tremor (e.g., Fee et al. 2010; Patrick et al. 2011; Thelen and Cooper 2014; Patrick et al. 2016). These gas pistoning cycles start with gas accumulation under the surface of the lava lake, limiting surface degassing and resulting in low seismic and infrasound amplitudes. The crust on the surface of the lava lake was typically dominated by large plates of solidified lava, which were pushed upward from accumulating gas beneath the crust. When the crust of the lava lake was breached by the shallowly stored gases, vigorous spattering then took place, driving rapid increases in the seismic and infrasound



Bulletin of Volcanology (2022) 84:76 Page 5 of 24 76

Fig. 2 Comparison of the 10-min infrasound parameter (black) to the 10-min median seismic amplitude at station NPT (gray). Note that the different panels have different limits to accentuate certain phenomena. Black dotted lines in **b** show composite events, blue dotted lines in **c** show proto-collapse events, while red dotted lines in **c** show collapse events. Data were bandpass filtered between 0.7 and 10 Hz



amplitudes. Spattering continued until the surface once again sealed itself to gas release, starting the cycle over again.

Rockfall and emission events

Visual observations by the HVO staff allow the characterization of two types of infrasound transients that can also be easily differentiated based on their frequency content. The first type was dominantly composed of infrasonic frequencies greater than 0.5 Hz and had an emergent cigar-like shape (Fig. 3a). The seismic signal was similarly rich in high frequencies, emergent, and cigar shaped. Visual observations of dilute dust plumes were common with these events, and hence were attributed to rockfall from the walls of Halema'uma'u crater onto the lake surface. The second type was enriched in lower frequencies, with a dominant peak between 0.2 and

0.3 Hz (Fig. 3b). The peaks were consistent between NPT (~1 km distant) and AHUD (~5 km distant), and there was often a high-frequency rockfall-like signal at the beginning of the event. Visual observations of these events showed larger, denser plumes, composed of ash and dust. In most cases, there was a radar-detectable plume at 2000 m or higher shortly after these events. Neither event was associated with a tilt transient. During the eruption, some of these events were internally called "Type-B" events; however, for this discussion, we are going to call these emission events to avoid confusion with the classification scheme of Minakami (1974). The consistent peak in frequency between 0.2 and 0.3 Hz (and another smaller peak at ~ 0.8 Hz) is interpreted here as an effect of the geometry of the conduit and crater, similar to interpretations invoking a Helmholtz resonator described in Fee et al. (2010).



76 Page 6 of 24 Bulletin of Volcanology (2022) 84:76

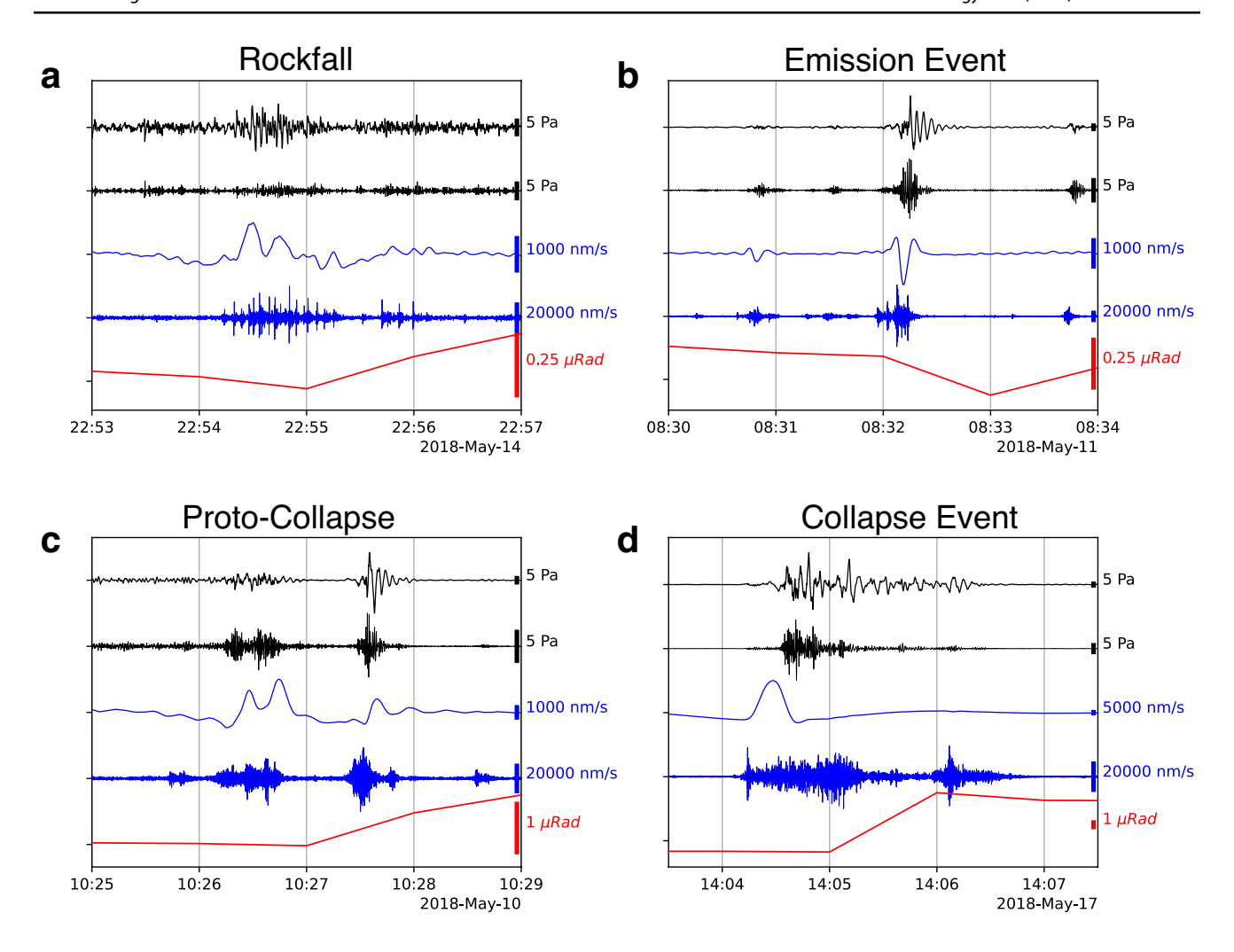


Fig. 3 Example rockfall, emission event, proto-collapse, and caldera collapse event in panes **a** through **d**, respectively. From top to bottom, the traces are band-pass filtered infrasound (0.1–15 Hz), high-pass filtered infrasound (>1 Hz), low-pass filtered seismic velocity (<0.1 Hz), high-pass filtered seismic velocity (>1 Hz), and radial tilt.

Infrasound and seismic data from station NPT. Tilt data from station UWE (Johanson and Miklius, 2019). An amplitude scale of each trace is at the far right, and the scales are variable for each plot to show the details of the waveform

Composite events

Composite events consisted of a broadband seismic signal derived from rockfall onto the lava lake surface and the response to that impulse (Patrick et al. 2011; Orr et al. 2012). They were commonly observed during the presence of a lava lake between 2008 and 2018 (Patrick et al. 2021). Composite events from 2008 to 2018 also had an infrasound transient, inflationary tilt offset recorded on the caldera rim and in some larger cases, a minor explosion, especially for the larger rockfall events (Poland et al. 2021b). The diverse geophysical transients bore a significant resemblance to subsequent collapse and protocollapse events.

Caldera collapse events

Caldera collapse events were large and geophysically conspicuous phenomena that largely defined the 2018 summit eruption. Each collapse consisted of the following characteristics (Figs. 3 and 4):

- (1) A broadband seismic transient, including VLP energy, with a magnitude of approximately M_w5 .
- (2) A broadband infrasound transient.
- (3) A step increase in radial tilt (inflation).
- (4) A downward offset in displacement within the caldera, as measured by GNSS instrumentation.



Bulletin of Volcanology (2022) 84:76 Page 7 of 24 76

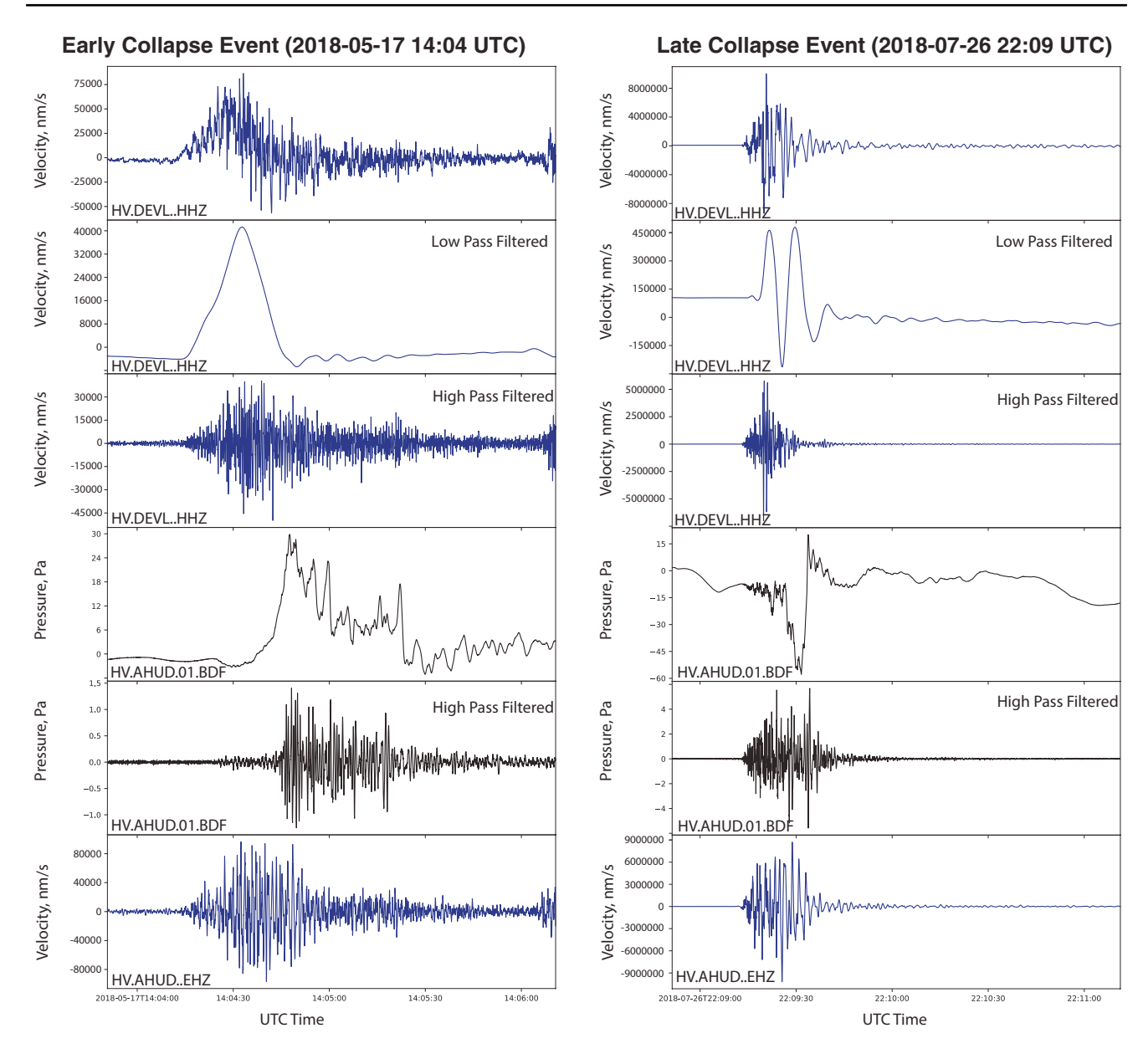


Fig. 4 Comparison of seismic (blue) and infrasound (black) waveforms from a collapse event early in the eruption (May 17, 2018; left) and late in the eruption (July 26, 2018; right). Note the different scaling of the waveforms on the left and right panes. From top to bottom: instrument corrected velocity waveform from HV.DEVL..HHZ lowpass filtered velocity waveform at < 0.1 Hz, high-pass filtered velocity

waveform at>1 Hz, instrument corrected infrasonic pressure waveform from HV.AHUD.01.BDF, high-pass filtered infrasonic pressure waveform, instrument corrected velocity waveform from HV.AHUD.. EHZ. Station DEVL was~5 km from the vent and remained on-scale for each collapse event

The event was followed by very low rates of seismic tremor and very low rates of earthquakes below the caldera. Tremor amplitudes, earthquake rates, and earthquake magnitudes all increased ahead of the next collapse event (Shelly and Thelen 2019; Tepp et al. 2020). GNSS, and eventually, visual observations made clear that the overall process for these events was episodic collapse; however, the details of the cycle and the processes responsible for the variety of geophysical observations require additional study. After

the first few events, the similarity to composite events in seismic, infrasound, and tilt observations was striking, and guided early interpretation as well as safety decisions regarding work in the summit area during the eruption.

Proto-collapse events

A subset of emission events prior to the first recognized collapse showed many of the same characteristics as the



76 Page 8 of 24 Bulletin of Volcanology (2022) 84:76

collapse events but exhibited smaller amplitude and less regularity in occurrence. These characteristics included an infrasound transient, a drop in the average seismic amplitude of the tremor, a rapid inflationary tilt signal, and a very-long-period (VLP) earthquake (Fig. 5). Given the similarities, we invoked a similar collapse-induced pressurization model as the more well-known collapse events (i.e., Neal et al. 2019; Shelly and Thelen 2019; Tepp et al. 2020). Here, we term them "proto-collapse cycles" because of their geophysical similarities to the larger collapse events and their occurrence before the first recognized collapses.

The relative timing of the seismic and tilt transients with respect to the emission events is variable (Fig. 5). There are examples of a VLP and tilt transient after several

emission events, suggesting, if the signals are linked, a top-down trigger starting with a collapse of the crater rim. There are also examples of emission events after a VLP and tilt transient, suggesting a bottom-up process (Chouet et al. 2010; Jolly et al. 2018). In still other cases, there is little infrasound associated with VLP earthquakes and tilt transients, suggesting that the processes responsible for the seismic and tilt signals were below the surface, most likely near the top of the magma column. Based on the continuation of deflationary tilt after the clogging of the conduit by rockfall, the top of the magma column was likely well beneath the surface by this time period (Anderson et al. 2019).

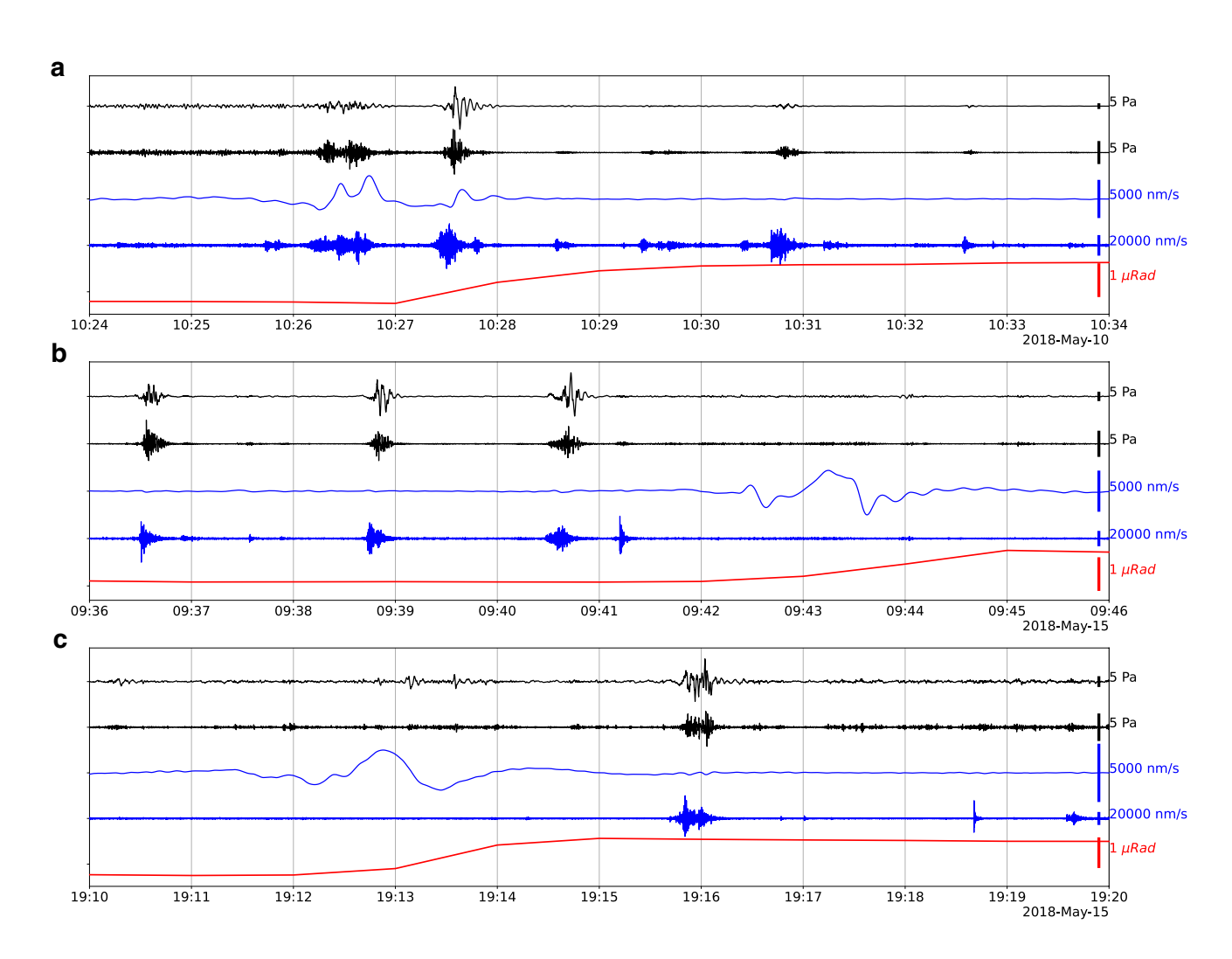


Fig. 5 Three proto-collapse events. In each plot, the black traces are the infrasound recorded on station HV.NPT. The top trace is high pass filtered above 0.1 Hz and the bottom black trace is high pass filtered above 1 Hz. The blue traces are the seismic velocity recorded on station HV.NPT. The top blue trace is low pass filtered below 0.1 Hz, and the bottom blue trace is high pass filtered above 1 Hz.

The red trace shows the radial tilt from the tiltmeter at Uēkahuna vault, assuming a source at Halema'uma'u. **a** Example of concurrent emission event, VLP, and tilt step. **b** An example of emission events preceding a VLP and tilt step, suggesting a top-down trigger. **c** An example of an emission event after a VLP and tilt step, suggesting a bottom-up trigger



Bulletin of Volcanology (2022) 84:76 Page 9 of 24 76

Summit chronology and discussion

One of the most common features of the seismic and infrasound recordings during the 2008–2018 summit eruption was the presence of gas pistoning events. In the days leading up to the 2018 eruption, the lava lake overflowed onto the floor of Halema'uma'u crater for only the second time during the 2008–2018 summit eruption. By analyzing the infrasonic tremor frequency during this time period and comparing it to periods when the lava lake was lower, we can assess the contribution of the conduit geometry and resonance on the recorded infrasound signal. Several common peaks in infrasound spectra between 0.4 and 0.8 Hz occur regardless of whether the lava level is low (within the conduit) or high (overflowing) (Fig. 6). Given common peaks in the spectra when there was an exposed conduit and when there was not, we can exclude conduit resonance as a potential source for the infrasound below 1 Hz. Similarly, Fee et al. (2010) described tremor during the early part of the summit eruption with relatively stable peaks from 0.3 to 0.6 Hz and from 1 to 3 Hz and did not see a change in resonance during short-duration drops in the lava lake. Instead, assuming resonating infrasonic wavelengths between 400 and 800 m, it seems that resonance of the larger Halema'uma'u crater is a more plausible source. Conduit resonance may explain

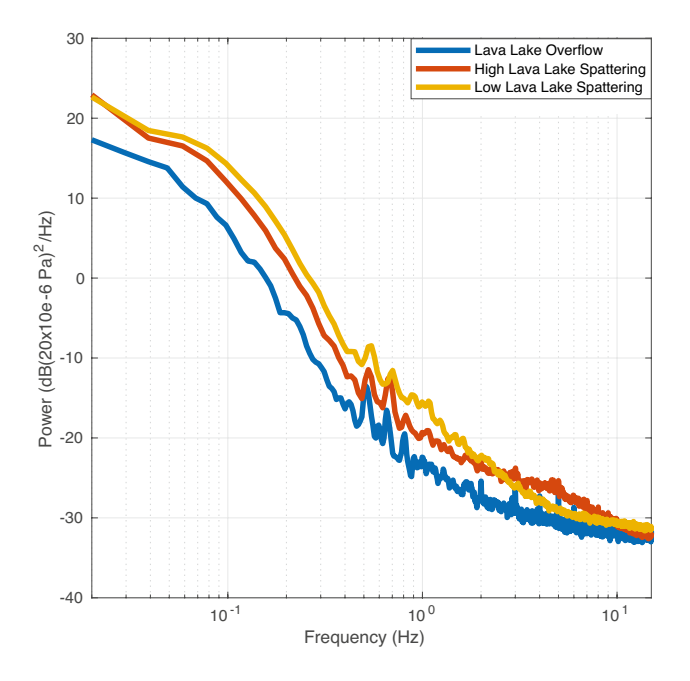


Fig. 6 Comparison of infrasound power spectral density (PSD) during overflow and spattering episodes. Each spectrum includes approximately 4 h of data. The time periods of analysis were 2018–04-26 16:21–20:16 UTC, 2018–04-26 12:21–16:21 UTC, and 2017–09-11 18:00–22:00 UTC for the overflow, spattering high lava lake, and spattering low lava lake, respectively

some minor peaks in the spectra just above 1 Hz, that were only seen when the conduit was exposed (Fig. 6).

On May 3, the lava lake began to drop in response to the dike intrusion and eruption downrift. Normal activity of the lava lake continued, including gas pistoning, until late in the day on May 5 UTC. After this time, the lava lake was in a nearly constant state of motion with chaotic degassing, facilitated in part by the collapse of unsupported, cooled lava pasted onto the sides of the conduit (Supplementary Fig. 2). Through this time, infrasonic and seismic tremor increased steadily (Fig. 2). Infrasound detections showed highly coherent back-azimuths toward the lava lake at Halema'uma'u, and the tremor was strong enough to obscure most of the observed rockfalls during this time period. On May 9 at 18:25 UTC, a series of two larger rockfalls occurred about 1 min apart that resulted in two composite seismic events: a two-microradian inflationary tilt and an explosion with a plume that extended to about 1800 m elevation (~800 m above the vent).

Increases in the amplitude of the infrasound signals between May 6 and 9 coincide with a transition in the lava lake surface from large plates to a highly disrupted surface with chaotic degassing (Fig. 2). The drop in lava lake elevations within the flared geometry of the conduit may also have served to amplify the infrasound signal (Johnson et al. 2018b). The increase in seismic amplitudes began around the time of the M6.9 South Flank earthquake on May 4, prior to the increase in infrasound amplitudes, and continued after the conduit became clogged on May 10.

The timing of the composite event on May 9 occurred at, or just after, the peak in infrasound tremor. Over the subsequent 16 h, the infrasound tremor amplitude dropped precipitously, despite a continued increase of the seismic tremor amplitude (Fig. 2). On May 10, there was a double composite event, at 10:26 and 10:28 UTC. Since the event occurred during darkness, there are no visual observations; however, there is a clear radar return at 2000 m elevation over the southwest side of the caldera, suggesting a plume similar to the event on May 9 was present. Shortly after the double event on May 10, infrasonic tremor dropped to background levels, and continuous infrasonic detections from the direction of Halema'uma'u ceased (Fig. 2). Further, no incandescence from the pit was observed, effectively marking the clogging of the conduit by debris preventing the magma column from direct interaction with the atmosphere. Seismic tremor did not change abruptly after the conduit was engulfed with debris, suggesting that the same processes that gave rise to the seismic tremor continued even after the conduit were buried.

The large-amplitude events on May 9 and 10 could either be classified as composite events or proto-collapse events. The only difference between the two is that a composite event has a rockfall trigger which can typically be confirmed



76 Page 10 of 24 Bulletin of Volcanology (2022) 84:76

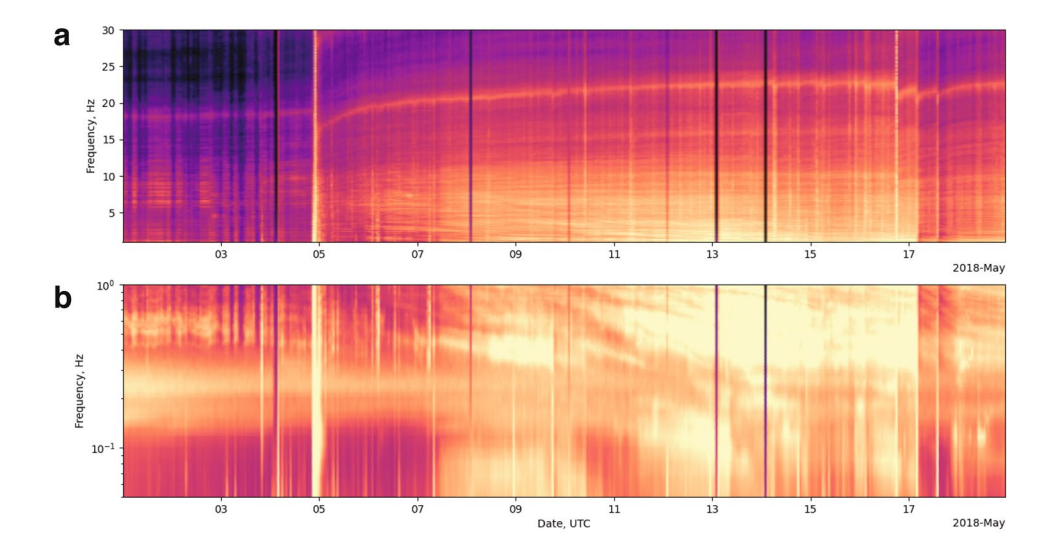
with a visual observation by a remote camera. Proto-collapses, on the other hand, do not have a known triggering mechanism.

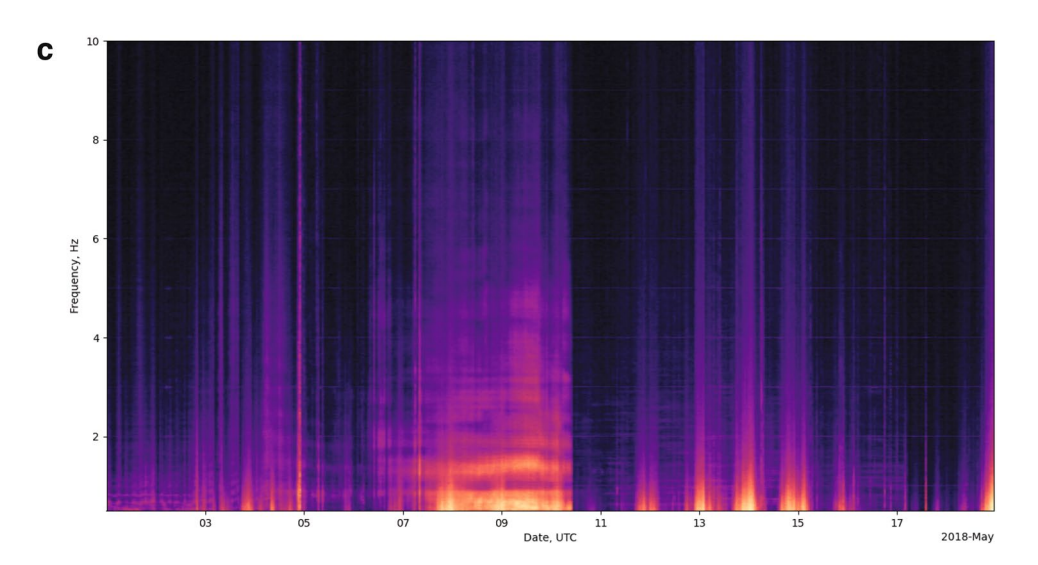
While spattering and degassing at the surface of the lava lake certainly contributed to the seismic tremor occurring at the time, the frequency content changed dramatically during the amplitude increase, suggesting multiple source processes and/or locations (Fig. 7). Seismic frequency content changes from the microseism to 25 Hz, including several gliding bands. One band between 15 and 20 Hz shifts rapidly after the M6.9 earthquake on May 4 and after the collapses starting on May 16. Infrasound frequencies are relatively constant. Further, while both the seismic and infrasound amplitudes were increasing at the same time, second-order changes in amplitude were not as well correlated as one would expect if the seismic tremor was entirely due to lava lake spattering, for example, during gas piston events. The additional source of the seismic tremor must also have been

deeper within the Halema'uma'u plumbing system, away from the impacts of a dropping lava lake level and beneath the ground where infrasound could not be generated.

Once the infrasonic tremor stopped on May 10, coherent infrasound detections were almost entirely reflective of discrete rockfall and emission events. Despite the presence of a buoyant and often ash-rich plume, continuous infrasound detections from Halema'uma'u crater were rare after the conduit became clogged by debris on May 10, occurring for approximately 5 h on May 13 and a few tens of minutes late on May 15. Seismic tremor frequencies between the microseism and 1 Hz increased markedly after the conduit closed (Fig. 7). The first recognized proto-collapse occurred on May 14 at 5:27 UTC (Fig. 2). Interevent times between proto-collapse events were irregular but occurred on the order of hours. The last recognized proto-collapse event was May 16 at 3:01 UTC, just over 24 h before the first recognized collapse event.

Fig. 7 Spectrograms of seismic and infrasound data at the summit of Kīlauea during increases in seismic and infrasonic amplitudes. Spectrogram of seismic channel HV.NPT..HHZ at high frequencies (a) and long periods (b). Spectrogram of infrasound channel HV.AHUD.01.BDF (c). All spectrograms use 60 s windows to calculate the spectra, then average those spectra for each hour, which is plotted as vertical lines here. Vertical streaking in HV.AHUD spectrogram is dominantly wind noise, especially after May 10. The M6.9 South Flank earthquake occurred at 22:33 on May 4 and can be seen in seismic and infrasound spectrograms







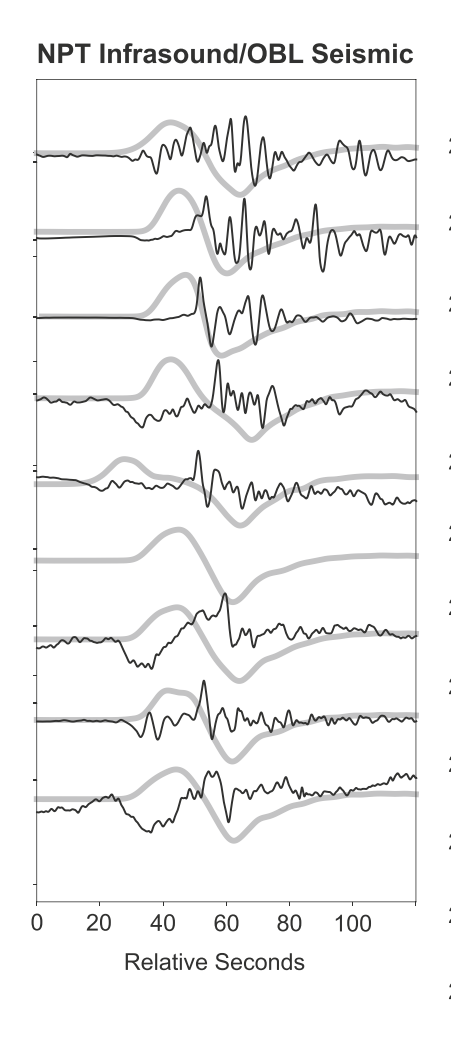
Bulletin of Volcanology (2022) 84:76 Page 11 of 24 76

Beginning on May 17 at 4:17 UTC, the first of 62 discrete caldera collapse events occurred (Neal et al. 2019). Based on the character of the seismic VLP and the infrasound waveforms, the first twelve events (May 17–26) were associated with an eruptive plume, one of which reached over 9 km above sea level. After the strong compressional infrasound arrival, dominant frequencies overlapped with emission events seen prior to the large collapses, consistent with large plumes observed from these events (Figs. 3 and 4).

All these collapse events are geophysical transients consistent with a "stomp rocket" model (Shelly and Thelen 2019) where collapse of a down-dropping piston pressurized a gas-charged magma chamber underneath. However, the question remains whether the same processes were responsible for the initial 12 collapse events, which were different from the subsequent 50 in terms of plume generation. We combined seismic and infrasound observations to constrain

failure mechanisms and timing for each of the initial 12 collapses. The tilt and GPS time series are too coarsely sampled (1 sample per minute or longer) and thus do not constrain the timing of collapse. In many of the events, the first obvious signal in infrasound is a strong compressional transient (Fig. 4). At frequencies above 1 Hz, the infrasonic amplitude built quickly and decreased slowly. These infrasonic observations were consistent with visual observations of a buoyant volcanic plume at the vent. Earlier in the infrasound record, however, there existed a subtle long-period dilatation at stations NPT and AHUD. At times, this dilatation was at or below the noise level of the trace. The consistency and causality of the dilatation were much clearer when the infrasound trace was time-shifted assuming a source near the vent and compared to the VLP band of the seismic data (Fig. 8). Time-shifting the infrasound data makes it clear that the infrasonic dilatation was present during each event

Fig. 8 Comparison of infrasound beam (black line) from NPT (left) and AHUD (right) to the seismic signal from station OBL (thick gray line) for each of the first twelve collapse events. NPT went down with the ship after the May 24 event, and thus, we use OBL for the comparison. NPT data were shifted by 2 s and AHUD data were shifted by 12 s to correct for the infrasound travel time to a source near the center of the initial collapses. Origin times for the initial 12 collapse events were not accurate enough to align the VLP phases, and thus, seismic and infrasound traces were further shifted together based on the maximum correlation of the VLP trace to align each of the collapse events



AHUD Infrasound/OBL Seismic 2018-05-17 4:15 UTC 2018-05-17 14:03 UTC 2018-05-19 9:58 UTC 2018-05-20 1:57 UTC 2018-05-20 21:49 UTC 2018-05-21 10:54 UTC 2018-05-22 3:50 UTC 2018-05-23 7:58 UTC 2018-05-24 4:43 UTC 2018-05-26 2:15 UTC 2018-05-26 10:44 UTC 2018-05-26 19:34 UTC 0 20 40 60 80 100 120 140 Relative Seconds



on at least one array and that it was coincident with the beginning of the compressional VLP signal.

Dilatations, or rarefactions, in infrasound are exceedingly rare; however, one simple explanation would be ground collapse. Other published examples of rarefaction onsets occurred at Cotopaxi (Johnson et al. 2018a) and Pu'u'ō'ō (Fee et al. 2011). At Cotopaxi, the signal was interpreted as crater floor collapse, and at Pu'u'ō'ō, the signal was attributed to downward motion of rockfall debris. Both processes are possible here; however, rockfall at the summit of Kīlauea typically has higher frequencies (Thelen and Cooper 2014). Rockfall can also be present in these collapse events, but frequencies consistent with rockfall do not occur until later in the event. Assuming that the dilatational first arrival is ground collapse, the infrasound-observed collapse is likely also responsible for the seismic VLP signal that starts at about the same time. Seismic VLP signals of similar character were commonplace in the 2008–2018 summit eruption and nearly always localized on the north side of the Halema'uma'u crater at a depth of approximately 1 km below the surface (Dawson et al. 2004). In the "stomp rocket" model of Shelly and Thelen (2019), the collapse compresses a pocket of exsolved gas at the top of the magma column and forces it out of the conduit tens of seconds later as seen in the compressional long-period arrivals on the infrasound records (Fig. 4). The subtle long-period rarefactions compare well with the small volumes of the initial collapses relative to later collapses (Fig. 4). Preliminary work estimated the collapse volumes based on the temporary infrasound recordings around the summit caldera (Fig. 1) and found smaller volumes than those calculated by differencing successive digital elevation models (Fee et al. 2018).

The collapse volume is likely the main difference between the proto-collapse cycles and collapse events. The collapse block progressively got larger with subsequent events between May 17 and August 2, 2018 (Neal et al. 2019). The presence of proto-collapse events extends the size progression backward in time to even smaller volumes, which help explain the smaller relative transient amplitudes and greater irregularity of the proto-collapse events compared to the well-recognized collapse events later in the eruption. The first collapse on May 17 did not just occur spontaneously, it was part of a progression that started with rockfall, expanded to composite events, and progressed to small collapses above a closed conduit in the weeks prior to May 17, 2018.

After the first 12 events, the collapse events became highly repetitive in the seismic VLP band and in long-period band of infrasound (<0.5 Hz; Fig. 9). The dilatation in infrasound became much larger, and the high frequencies were much shorter in duration (Fig. 10). This is consistent with the lack of an observed volcanic plume after the collapse event on May 26. Tilt and GPS transients also became stronger. The high-frequency seismic energy

increased significantly, whereas the high-frequency seismic energy was very weak before, considering the magnitude of the earthquake. The amplitudes became large enough to impact the infrasound records, creating shaking at the sensor, which can be seen in Fig. 4 as infrasound occurring at the same time as the direct seismic arrival. At high frequencies, the infrasound and seismic wave envelopes have nearly equal duration. High frequencies can also be seen in the raw infrasound signal preceding the large rarefaction. As in the initial 12 collapses, there is a strong positive pressure transient immediately after the rarefaction; however, given the lack of a volcanic plume, this is most likely a byproduct of the collapse process.

Lower East Rift Zone infrasound

In this second part, we focus on events and infrasound records for the LERZ. As for the summit events, we will first discuss the nature of explosions associated with lava fountaining at fissure vents, explosions associated with lava flowing into the ocean (littoral blasts) and lava fountaining, followed by a chronology and discussion of the eruption. Unlike the summit eruption, there are ample ground-based observations that can help tie infrasound tremor and transients to specific processes with a high degree of confidence.

Explosions

Immediately after infrasound was established in the LERZ, infrasound observations associated with fissuring activity was evident (Fig. 11). Activity was characterized by lowlevel infrasonic tremor with energy dominantly below 7 Hz that was punctuated by high-amplitude, short-duration transients that we interpret, based on visual observations, as explosions (Fig. 12). The infrasound transients associated with explosions were often composed of a highly similar, single cycle with an up first motion and a frequency around 3 Hz. Back-azimuths were consistent with a source near fissure 17 (see map in Gansecki et al. 2019). The lava erupted from fissure 17 was an anomalous crystal-rich andesite, giving it a higher viscosity and resulting in more explosive eruption style (Gansecki et al. 2019) than is typical for Hawaiian fissure eruptions. At the vent, activity was characterized by fountaining approximately 50 m high with occasional bursts to 100 m. In addition, there were ample photographic, video, and eyewitness accounts of small explosions incorporating steam and/or magma fragments, sending ballistics up to 400 m high (Gansecki et al. 2019; HVO Internal Logs).



Bulletin of Volcanology (2022) 84:76 Page 13 of 24 76

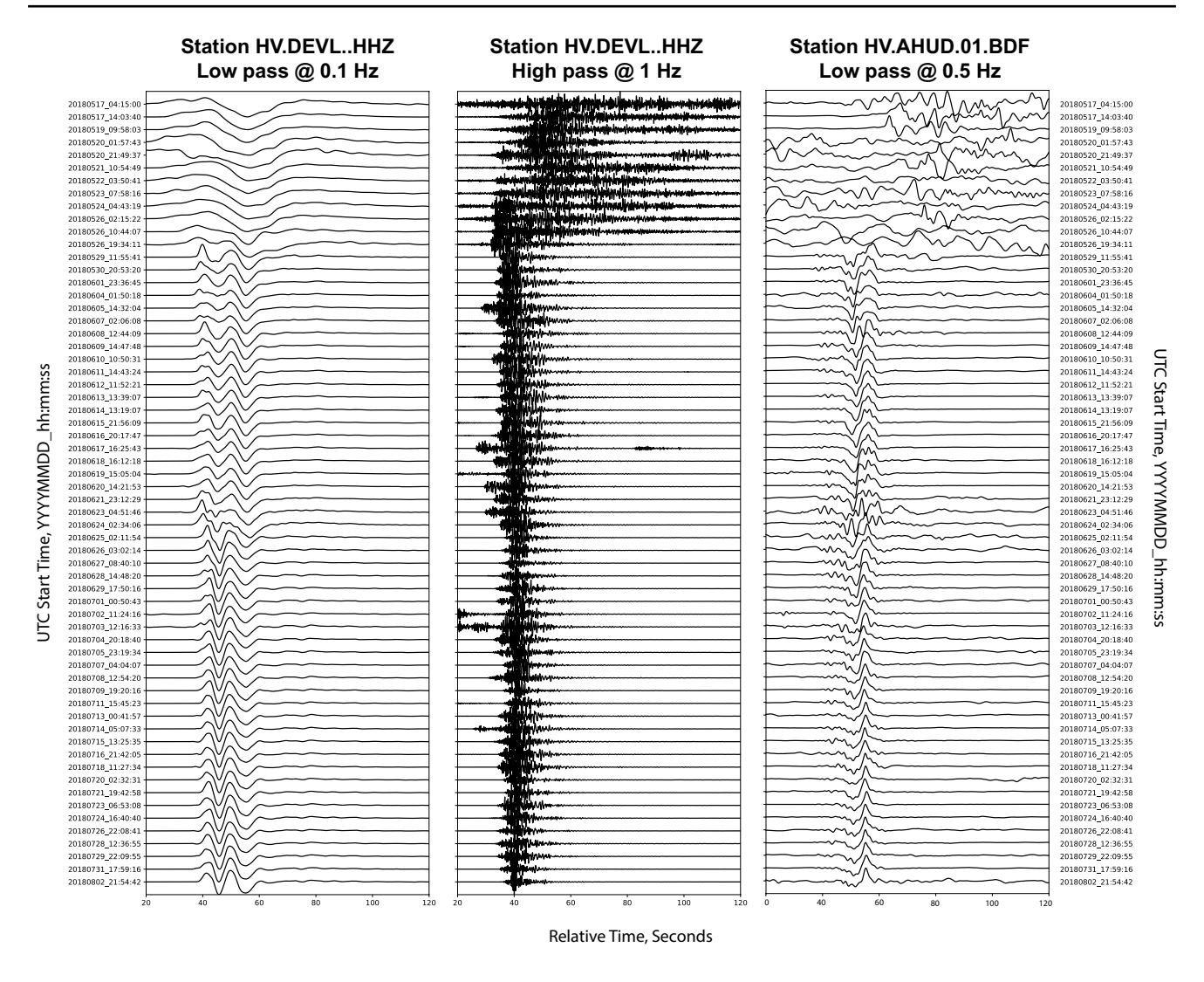
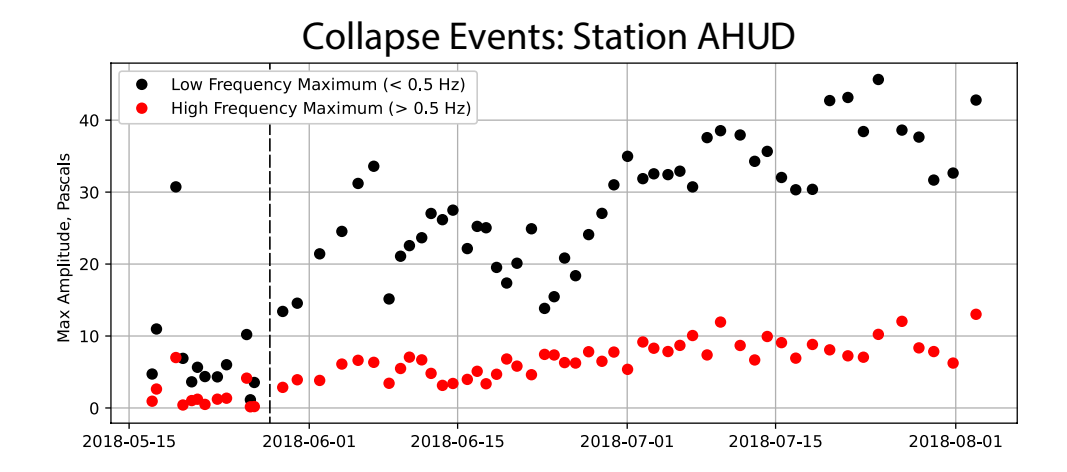


Fig. 9 Record section of seismic and infrasound for each collapse event. Left: Low-pass seismic traces from DEVL. Middle: High-pass seismic traces from DEVL. Right: Low-pass infrasonic traces from

AHUD. Traces are normalized individually. Traces in all three record sections are aligned according to the lags of the seismic VLP traces, using the collapse event on June 9 as the master event

Fig. 10 Maximum amplitude of the infrasound beam from station AHUD. Black dots are maximum amplitudes of the low-pass filtered beam, and the red dots are maximum amplitudes of the high-pass filtered beam





76 Page 14 of 24 Bulletin of Volcanology (2022) 84:76

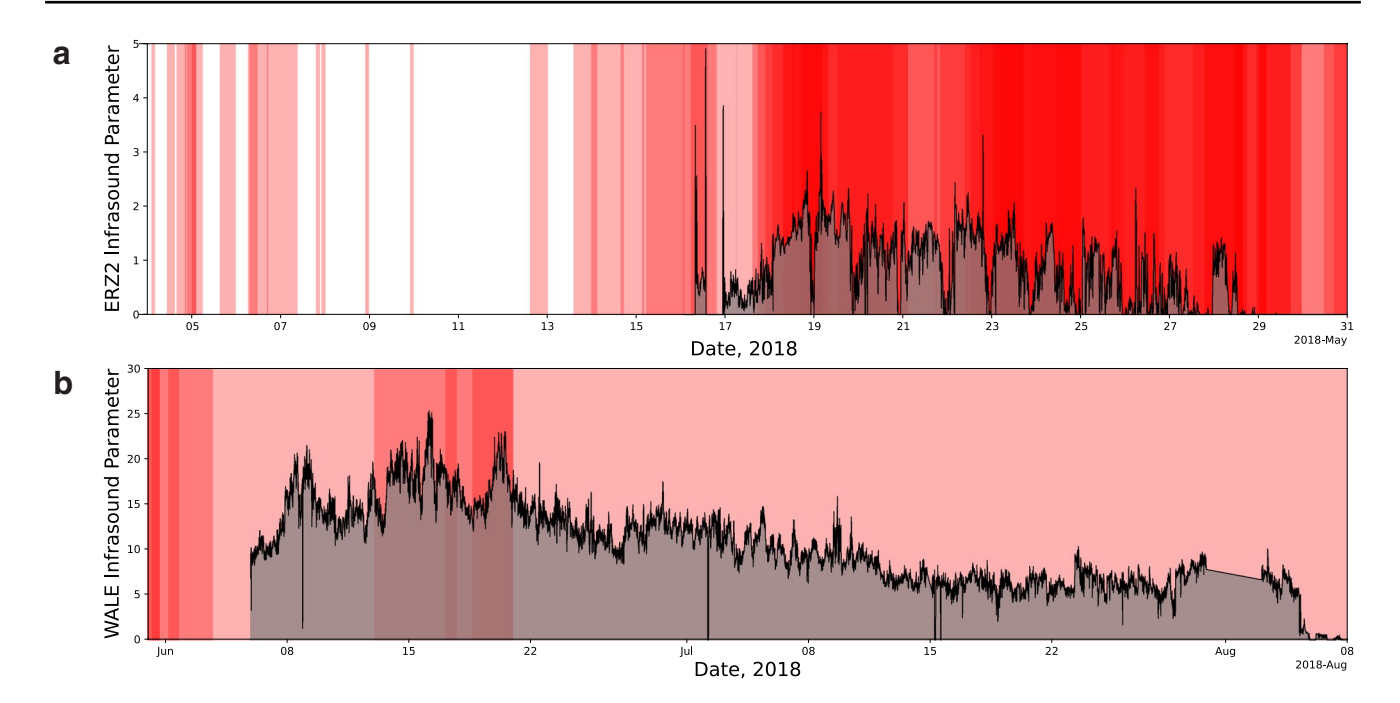


Fig. 11 Ten-minute Infrasound Parameter (IP) on station ERZ2 (a) and WALE (b) are plotted as a black line with gray filled below. Red rectangles show the duration of different fissures in the lower East Rift Zone. Overlapping rectangles result in a deeper red and show time periods where several fissures were active at the same time.

Data were bandpass filtered between 0.7 and 10 Hz. Azimuth ranges encompassed the range of fissures (255 to 285° for ERZ2, 104–194° for WALE). Time periods are shown to include the entire eruption and thus time periods when no proximal infrasound data was available, or data was not sufficient to obtain a back-azimuth

Littoral blasts

Another type of infrasonic transient was observed; this type also explosive in nature, but with a back-azimuth that pointed to an area where lava was entering the ocean. Once lava began flowing into the ocean, seismic tremor increased on several stations in the LERZ. The infrasonic signature of these ocean entries mostly consisted of impulsive explosionlike signals that were preceded by a low-frequency seismic signal (Fig. 13). Back-azimuths of the infrasonic explosions point toward the location of the ocean entry, and the difference in time of arrivals between seismic and infrasound signals suggests a source approximately 3 km away from station ERZ2, assuming a concurrent source of the seismic and infrasound signals. Our interpretation is that the high-amplitude seismic and infrasound transients described here are from littoral blasts at the ocean entry. Acoustic observations of explosions from the Kamokuna ocean entry in 1998 are detailed by Caplan-Auerbach and Duennebier (2001) using a hydrophone, but the signals are not directly comparable to our observations here.

Lava fountaining

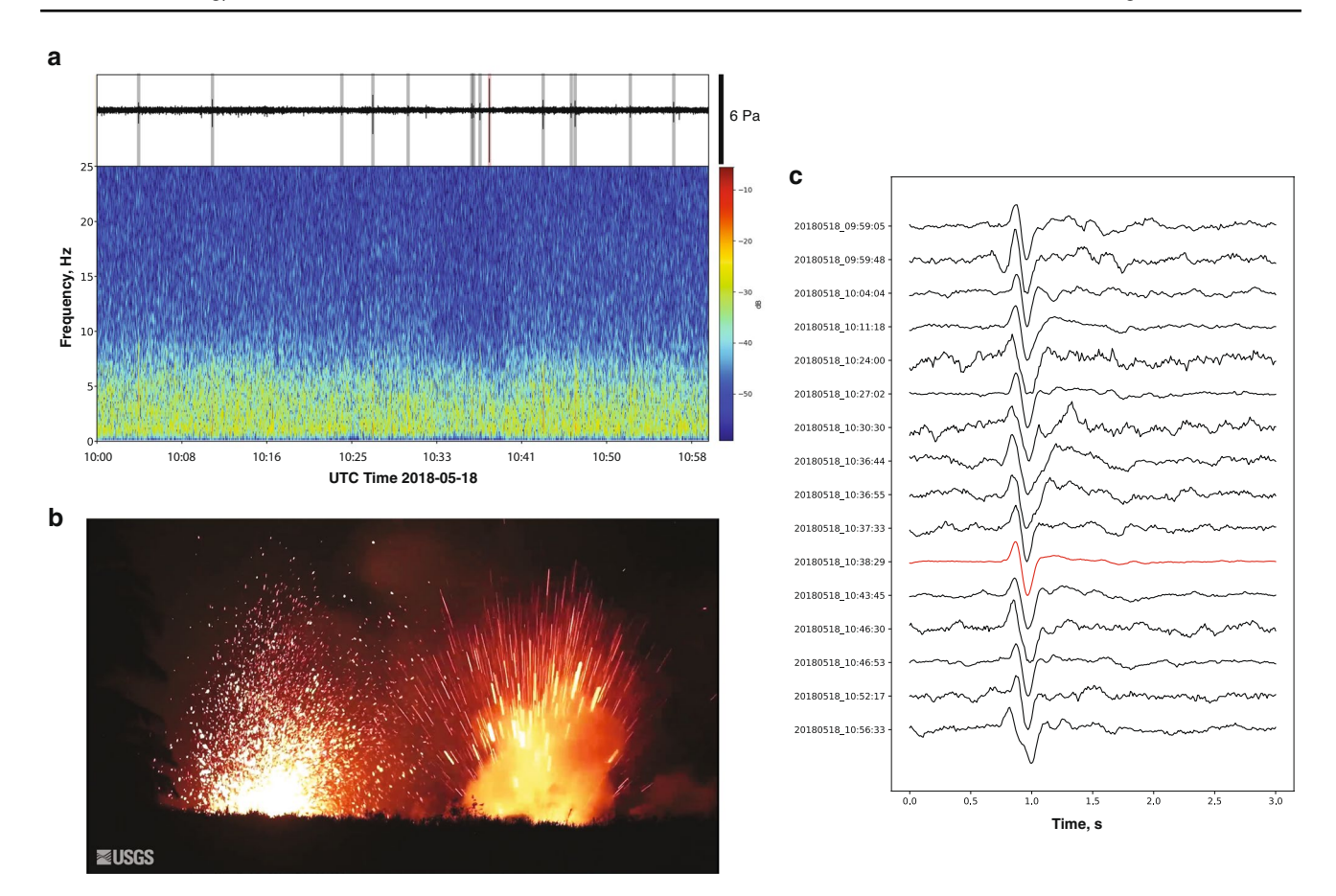
Infrasonic tremor was common during the LERZ eruption and typically had back-azimuths pointing in the direction of active fountaining or vigorous gas release. The infrasonic tremor had frequencies between the microbarom and about 7 Hz, regardless of the station (Figs. 12 and 14). Especially once the activity localized at fissure 8, the infrasonic tremor had very stable spectra and generally decreasing amplitudes with time (Fig. 11). Gestrich et al. (2021) analyzed the infrasound frequency content of the fissure 8 fountaining and found a good correlation with jet noise, suggesting a jet-like source mechanism.

LERZ chronology and discussion

At the Pu'u'ō'ō vent, the initial dike intrusion downrift was accompanied by a minor fissure eruption on the west flank of Pu'u'ō'ō and subsequent collapse of the Pu'u'ō'ō vent on May 1 (Neal et al. 2019; Poland et al. 2021a). There was no clear evidence of either collapse or fountaining on the AHUD or NPT infrasound arrays, which were the only operational arrays at the time, located 15-20 km away from the Pu'u'ō'ō vent. Array detections were instead fixed on the Halema'uma'u crater, which dominated the signal. Beamforming assuming a source at Pu'u'ō'ō also did not yield any significant amplitude transient. At other times during the eruption, detections were recorded from a back-azimuth consistent with Pu'u'ō'ō and/or fissures in the lower East Rift Zone (LERZ), but only during periods of light winds, typically at night. Three possibilities are thus likely, though they are not mutually exclusive:



Bulletin of Volcanology (2022) 84:76 Page 15 of 24 76



transport.

Fig. 12 Overview of fissure 17 activity. **a** Spectrogram from ERZ2 with waveform above showing typical fissuring tremor at fissure 17 punctuated by high-amplitude transients. Detected events are shown with a vertical gray line. Red vertical line corresponds to the red event in **c**. **b** Image extracted from video taken on May 18, 2018, at approximately 20:30 UTC. On the left is the typical fountaining activity responsible for the infrasonic tremor, and on the right is an

explosion, which is thought to be responsible for the high-amplitude transients. Fountaining on the left is on the order of 50 m during this time period, though no estimate was given for this exact time period of the image/video. Original video can be found in the supplementary section to this paper. c Record section of high-amplitude transients seen in a as recorded on ERZ2. The red waveform corresponds to the explosion seen in b. Amplitudes are normalized

- (1) The strength of the signal from Halema'uma'u crater overwhelmed the signal arriving from Pu'u'ō'ō,
- (2) The propagation and/or noise levels were unfavorable for detections from that back-azimuth (Fee and Garces 2007), and
- (3) The fissuring on the west flank of Pu'u'ō'ō was weak and the collapse of the Pu'u'ō'ō crater was slow.

Indeed, cloudy conditions prevailed during the fissuring and collapse at Pu'u'ō'ō, obscuring views from nearby webcams or other ground-based or airborne visual observations.

On May 4 at 2:50 UTC, the first fissure broke the surface in the Leilani Estates Subdivision in the LERZ. At the time of the eruption, the LERZ was sparsely instrumented, with a limited set of seismic and geodetic equipment (Shiro et al. 2019). At the beginning of the LERZ eruption, the nearest infrasound sensor was located approximately 40 km away at the summit of Kīlauea (AHUD). During the initial

fissures, spattering was too weak to be recorded by the existing infrasound arrays. Initial fissures did have seismic signals associated with them, especially on the two closest stations (KLUD and PHOD) but the infrasound and ground coupled airwaves associated with the fissuring are inseparable from the seismic signals associated with shallow magma

It was not until May 16, 2018, that the first infrasound array was installed in the LERZ at a location 4–8 km south of the fissures (ERZ2; Fig. 1). Between May 16 and 19, several fissures were active (4, 6, 13, 15, 16, 17, 18, 20, 21, 22, 23); however, most coherent signals recorded on ERZ2 arrived in a direction closest to fissure 17, approximately 4 km away. High-amplitude infrasound transients associated with explosions over a background of infrasonic tremor associated with low-level fissuring were common. Utilizing the similarity of explosion signals, we used a large event to perform a matched filter to detect additional explosions



76 Page 16 of 24 Bulletin of Volcanology (2022) 84:76

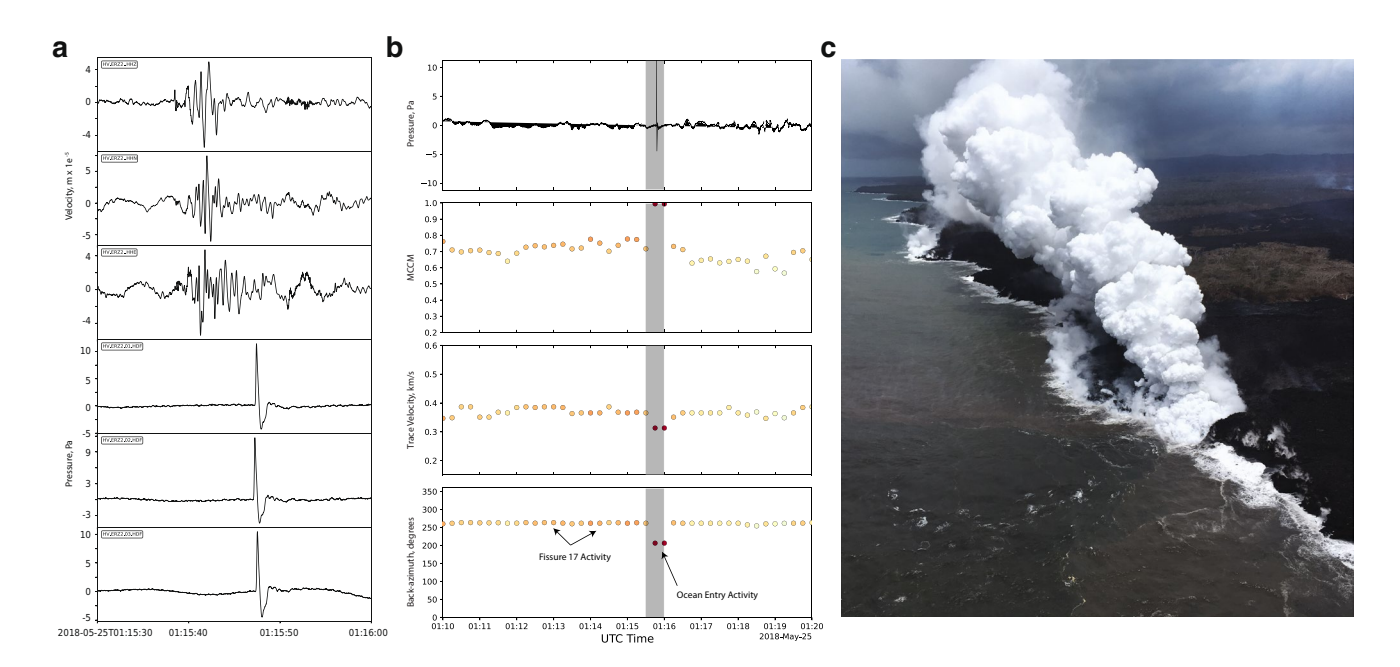


Fig. 13 Recording of a littoral blast from the ocean entry on May 25, 2018, UTC. **a** Seismic recording from ERZ2 (top three traces) and infrasound recording (bottom three traces). **b** Example of a littoral blast detection. Top pane: Unfiltered ERZ2 waveform. Middle top: MCCM for each 30-s window with 50% overlap. Middle bottom: Trace velocity of each 30-s window. Bottom pane: Back-azimuth for

each time window. The gray vertical rectangle shows the time period shown in **a**. Each circle is with respect to the MCCM. **c** USGS photo of the ocean entry on Saturday May 26, local time. The plume in the foreground is estimated to be at least 100–300 m wide where the lava is interacting with the ocean

(Fig. 12). In the infrasound data, these transients occur several and sometimes several tens of times an hour early in the analysis window (Fig. 15). Maximum recorded amplitudes of the recorded explosions range from 0.2 to 100 Pa with most transients between 0.3 and 5 Pa. Activity at fissure 17 waned along with the number of detected explosions until the end of activity at fissure 17. Some detections did occur after the observed cessation of activity, but they have very low rates of occurrence.

Beginning May 18, the locus of activity shifted westward creating new fissures (18, 19, 20, 21, 22, 23, 24) and reactivating older fissures (3, 7, 8, 9, 13, 14, 15, 16). This progression is well captured in the infrasound record, despite the limited azimuthal difference between fissures (Fig. 16). Our analysis only captures the most dominant coherent signal in the recorded waveform. It may be possible to more carefully detail the progression of westward fissuring by using an array processing algorithm that can separate multiple coherent signals occurring at the same time or by using more limited bandpasses (e.g., Goldstein and Archuleta 1987; den Ouden et al. 2020; Iezzi et al. 2022).

As fissure activity moved west, the erupting lava became much less viscous (Gansecki et al. 2019), flowing southward from the fissures to the ocean. Around midday on May 20 UTC, lava reached the ocean from fissure 20. Eventually, fissures 6, 13, and 22 also produced flows that fed concurrent ocean entries, all to the south of the fissures. Shortly

after the ocean entry was established, seismic and infrasound transients associated with littoral blasts began to be observed. Using back-azimuths calculated on station ERZ2, we can see that the number of detections from the ocean entry (200–225°) coincides well with the observed activity at the ocean entry (Fig. 15). Transients had maximum recorded amplitudes of less than 10 Pa, with most observed detections below 1 Pa maximum amplitude. The event rate of transient detections associated with littoral blasts is not constant, but highly irregular, suggesting that the conditions for littoral blasts may be more complicated than simply lava flowing into the ocean. By May 27, activity at the ocean entry had largely diminished or ceased altogether.

Activity eventually concentrated at fissures 7 and fissure 8 in late May, which sent lava northward. During this time period, one of the three elements in the ERZ2 array became noisy, compromising the calculated back-azimuths. Data after May 30 were improperly archived and lost. Thus, no infrasound array data were available until WALE was installed on June 5. By June 8, the activity at fissure 8 had intensified from Hawaiian lava fountains to strombolian type activity. The WALE array lies about 4 km north of the cone of Ahuʻailāʻau (fissure 8), and the array data were dominated by tremor coming from the direction of the large fountain.

Patrick et al. (2019a, b) described two time scales of transients associated with amplitude changes in the infrasound recorded from fissure 8. The first were short-term



Bulletin of Volcanology (2022) 84:76 Page 17 of 24 76

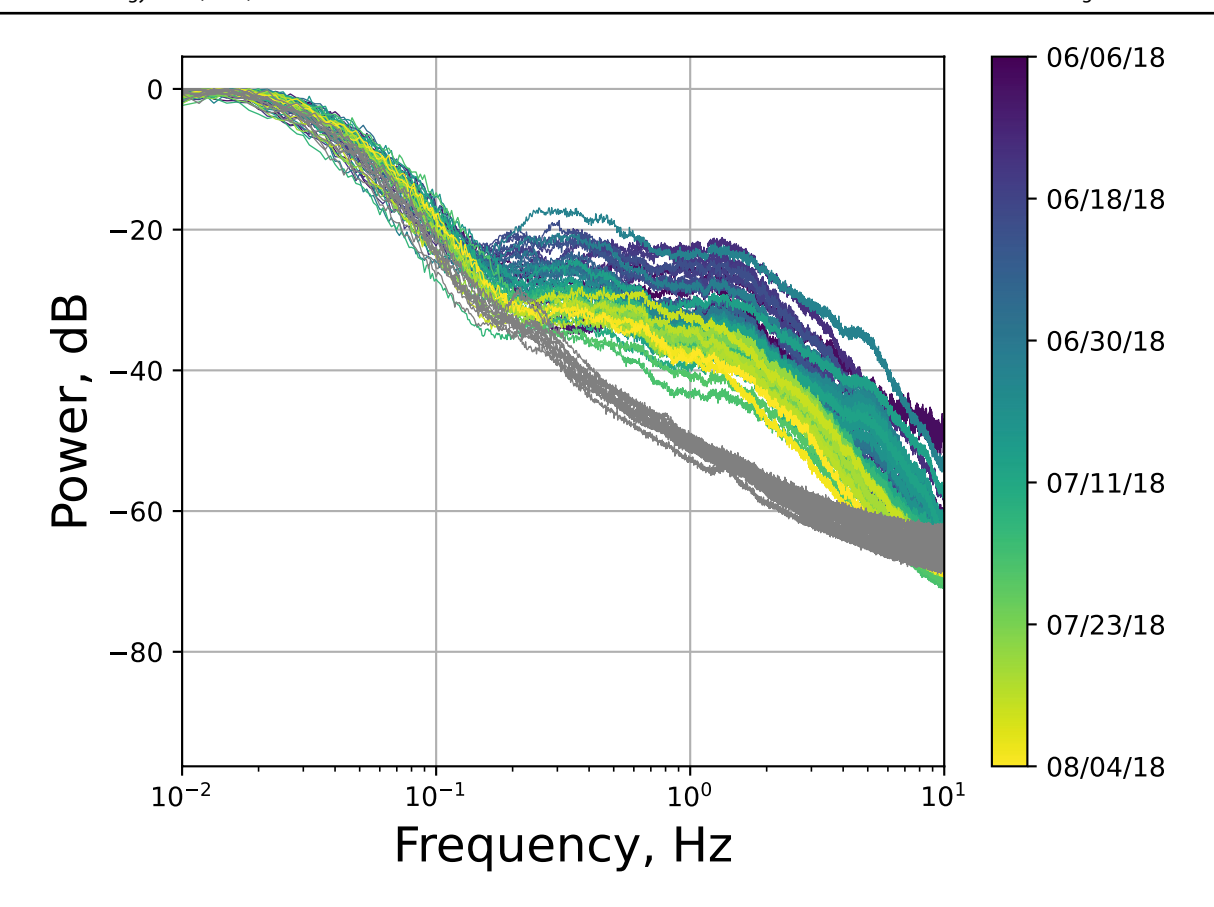


Fig. 14 Infrasonic spectra of lava fountaining at fissure 8 recorded on station WALE. Spectra are calculated over 10-min time segments with 50% overlap. Each line above is a day of 10-min spectra averaged together. Lines are color coded by date with earlier spectra

shown in dark blues and later spectra shown in greens and yellows. Gray spectra represent the "background" spectra calculated between August 10 and 20. Background spectra are calculated and averaged exactly the same as the colored spectra

cycles of up to 10 min where the increases in the bulk effusion rate from the fissure 8 vent corresponded to decreases in the seismic and infrasound amplitudes. Patrick et al. (2019a, b) attributed the relationship to a difference in degassing efficiency and foam formation sometimes seen in gas pistoning. They suggested that the extrusion rate was nearly constant across the short-term variations in infrasound and seismic amplitudes. This activity only occurred for about 2 weeks between July 14 and 29 and was not characteristic of the overall fissuring activity at fissure 8.

The second time scale occurred on the order of days and is associated with collapse events at the summit of Kīlauea. Within minutes of a collapse at the summit (~40 km away), amplitudes of seismic and infrasonic tremor increased rapidly (hours) with a slower decline in amplitude (tens of hours). Patrick et al. (2019a, b) attributed these changes in seismic and infrasonic amplitudes to enhanced fissuring and extrusion caused by an increase in pressure from the summit collapses. Interestingly, Patrick et al. (2019a, b) pointed out that effusion rate changes from summit collapses, and the changes in infrasound amplitudes were not present until mid-June and in early- to mid-July.

Lyons et al. (2021) further investigated the infrasound generated during both the short-term and long-term changes in effusion rate at fissure 8, using the campaign data (5L. FIS8; Fig. 1) recorded 500 m from the vent. They detailed changes in back-azimuth that moved from the vent direction down the proximal lava channel, or spillway, when effusion rates increased. Field observations and unoccupied aircraft systems (UAS) imagery showed that during the periods of high effusion rate, the flow would become turbulent in the spillway and breaking waves would form in the lava flows. Lyons et al. (2021) found that the spectral content of the spillway infrasound varied from the vent infrasound and proposed that the source of the spillway infrasound was primarily the interaction of the turbulent lava free surface with the atmosphere.

Notably, while fissure 8 was the dominant vent from early June until the end of the eruption, it was not the only active fissure. Fissures 16, 22, and 6 were all reactivated in parts of June or July. When activity at fissure 8 was subdued, signals from other active fissures and/or ocean entries could occasionally be detected. One such signal occurred on July 16 around 15:33 UTC (5:33 local) when a tour boat was



76 Page 18 of 24 Bulletin of Volcanology (2022) 84:76

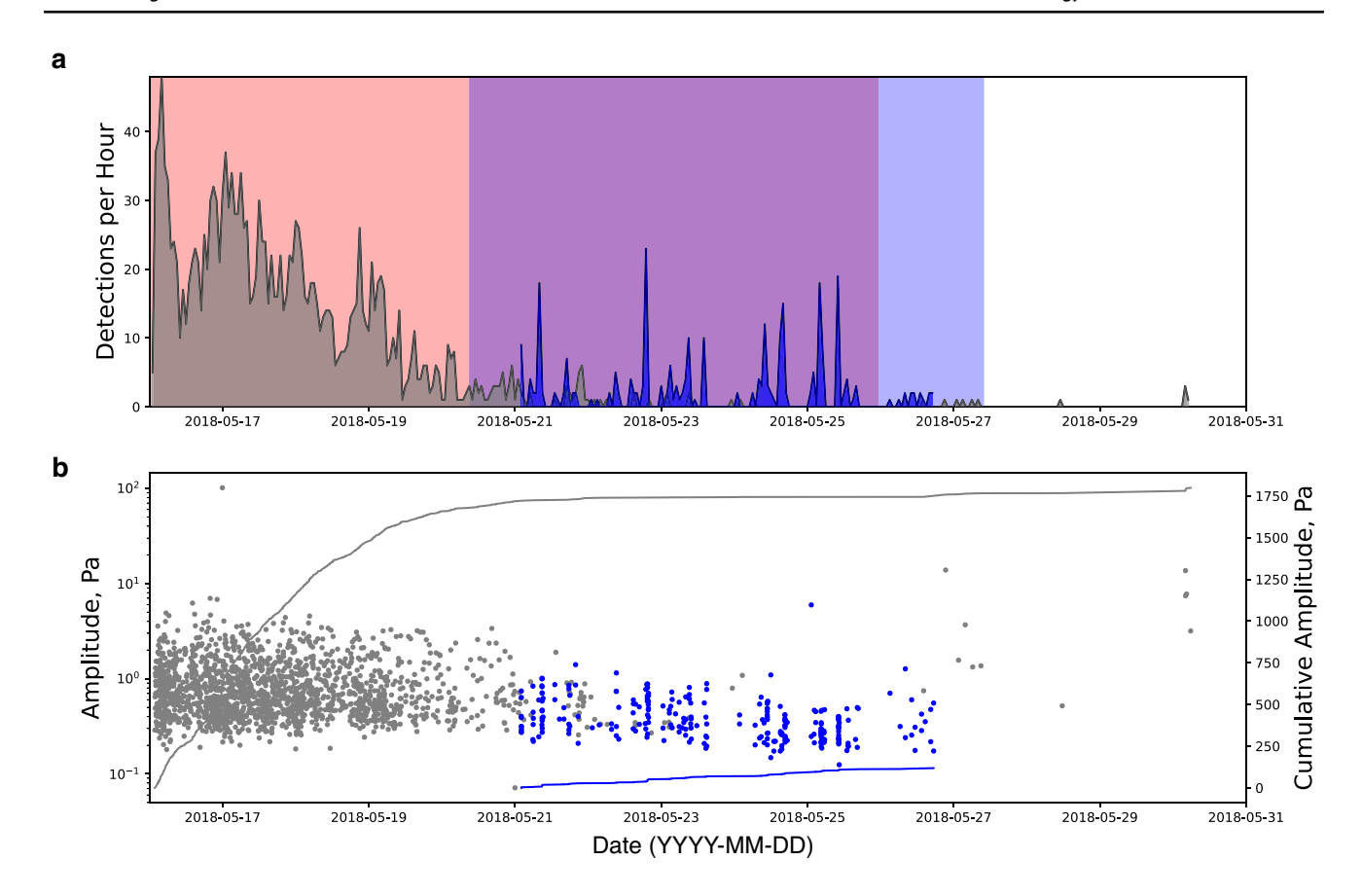
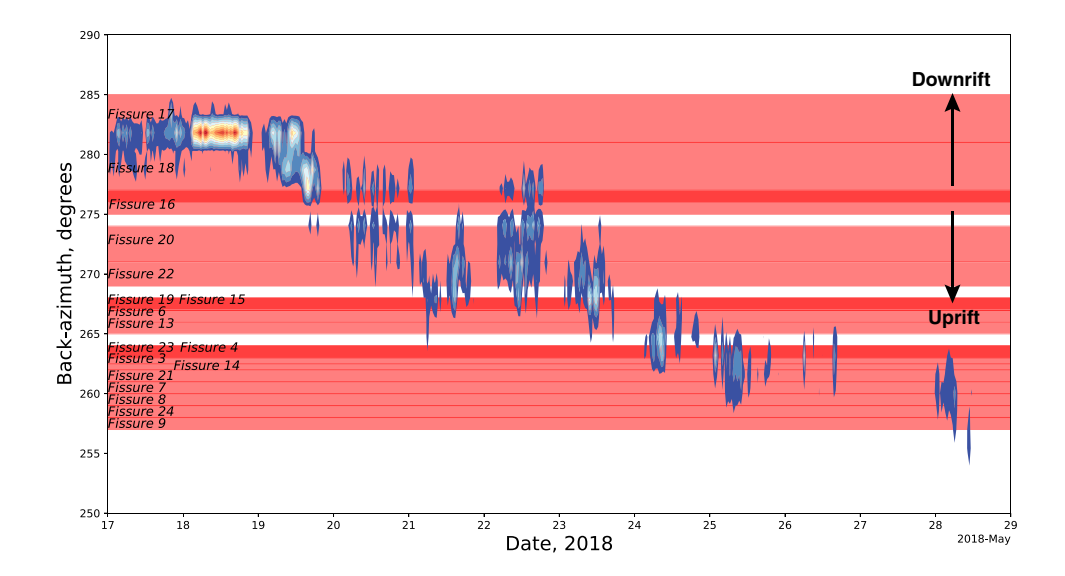


Fig. 15 Time series of explosions from fissure 17 (gray) and littoral blasts (blue). **a** Event rate plot of explosions (gray) and littoral blasts (blue). Explosions were detected using a matched filter with the red waveform in Fig. 12c. Littoral blasts were defined as high-amplitude transients with back-azimuths calculated on station ERZ2 originating from the direction of the ocean entry (200–225°). The red box shows

the duration of fissure 17, while the blue box shows the duration of the southern ocean entry. **b** Max amplitude of the detected signals as recorded on ERZ2. Gray dots represent individual events, and the gray line shows the cumulative amplitude. Blue dots represent max amplitudes of impulsive detections from the ocean entry and the blue line is the cumulative amplitude

Fig. 16 Weighted sum of coherent detections from HV.ERZ2. Detections with an MCCM parameter > 0.6 and relative velocities between 0.25 and 0.45 km/s were considered in this analysis. Warm colors indicate more detections from a given back-azimuth, while cool colors indicate fewer detections. Sums are weighted by the MCCM





Bulletin of Volcanology (2022) 84:76 Page 19 of 24 76

struck by ballistics from a littoral blast injuring 23 people (https://www.nytimes.com/2018/07/17/us/lava-bomb-boat-video-hawaii.html). The blast was recorded above the fissuring tremor of fissure 8, and array processing reveals a back-azimuth consistent with the site of the blast. The infrasound signal is more complex than the example in Fig. 13 and consists of 4 pulses of declining energy extended over approximately 30 s.

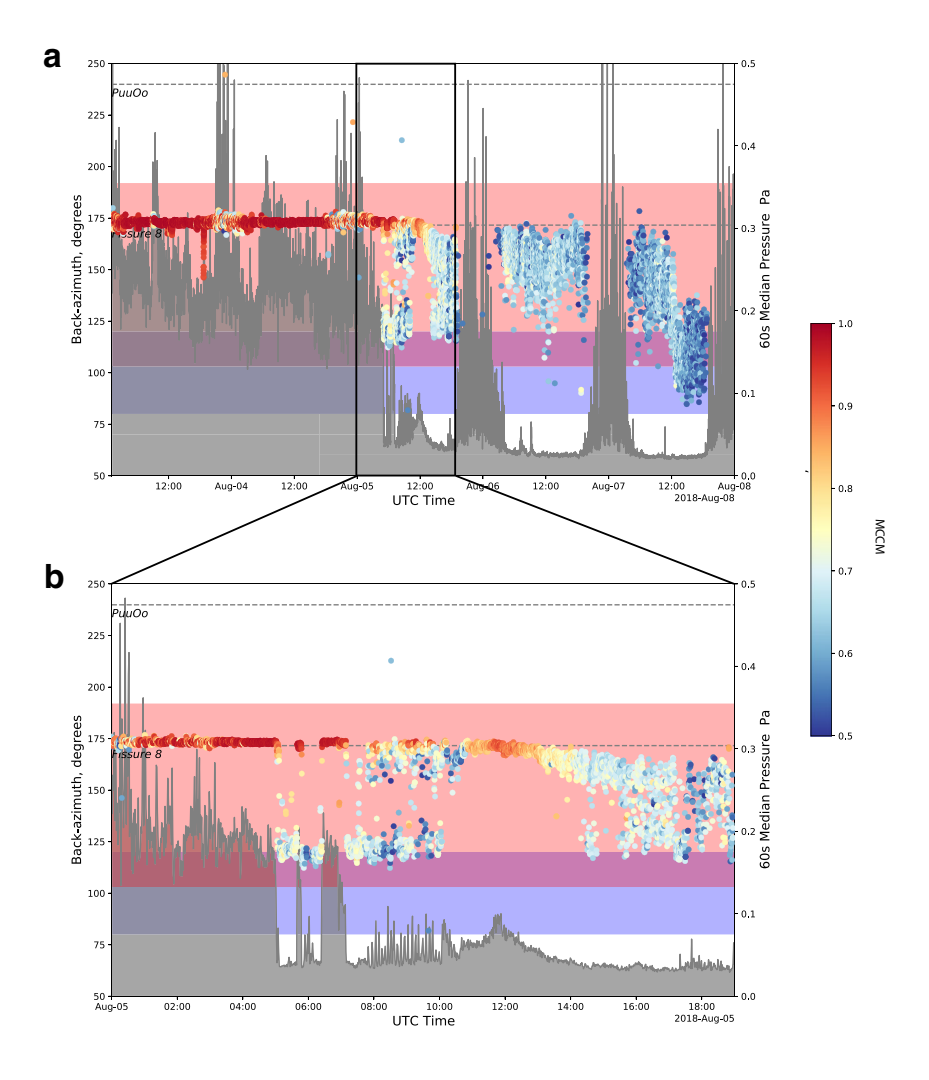
The end of the 2018 eruption in the lower East Rift Zone is not easy to pinpoint. Vigorous fissuring stopped on August 5 (August 4 local) and fresh lava was not seen again in the main channel exiting the vent except within the cone between September 1 and 4. However, the recorded infrasound tells a more complicated story. Decreases in the rate of effusion of lava were reported at fissure 8 beginning in the end of July. There was a data outage at WALE between July 31 and August 2; however, infrasound amplitudes maintained similar levels observed over the previous 2 weeks (Fig. 11). Infrasound amplitudes at the vent decreased rapidly to levels below the detection threshold of WALE by 5:05 UTC on August 5 (August 4 19:05 local) (Fig. 17). During

the decrease in infrasound amplitudes, seismic amplitudes also decreased, and visual observations documented that the lava was ponded and crusted over within the fissure 8 cone, with only a small roiling fountain present. Coherent tremor consistent with degassing or fissuring at fissure 8 occurred between 5:39–5:48 UTC and 6:24–7:10 UTC on August 5. Then, between 7:30 UTC and 10:00 UTC, there was pulsating tremor coming from the direction of fissure 8, then a lower amplitude tremor signal with constant amplitudes until around 16:00 UTC (Fig. 17).

Interestingly, when the infrasound signals from fissure 8 waned on August 5, the WALE array detected coherent signals from back-azimuths spanning all the previous fissures to the east of fissure 8 and the active ocean entry. Using the FIS8 array together with the WALE array suggests that breaking ocean waves distributed along the coast are likely sources, made louder by the passage of Hurricane Hector around August 8 (e.g., Garces et al. 2003; Le Pichon et al. 2004; Lyons et al. 2014).

Field observations of activity at the fissure 8 vent continued to show a decrease in activity, and by August 17,

Fig. 17 a Plot of back-azimuths (colored circles) calculated from station WALE at the end of observed fissuring. Colors of the circles are based on the MCCM. Warmer colors indicate higher coherence and thus more precise back-azimuth calculations. Only back-azimuths with an MCCM value of greater than 0.5 and an apparent velocity between 250 and 450 m/s are plotted. The gray line and shaded area represent the 1-min median pressure between 0.8 and 10 Hz calculated with the 02 channel of the WALE array. Clear diurnal noise is present in the median signal. The red shaded rectangle represents back-azimuths of previously active fissures, and the blue rectangle represents the backazimuths of the ocean entry. Dotted horizontal lines show back-azimuths to fissure 8 and Pu'u'ō'ō. b Same as a, except zoomed in on the end of fissuring on August 5 UTC





there was no incandescence observed. Regardless, coherent infrasound was detected from the direction of fissure 8 on August 9 from 5:10 UTC until late in the day on August 12. Coherent activity consisted both of tremor and short high-amplitude transients. Subsequent detected activity from fissure 8 was highly inconsistent, and usually consisted of minute-long tremor bursts. Field crews did note the presence of intermittent gas jetting from vents and hornitos in the spatter cone. Active lava again was visible on the floor of the fissure 8 cone between September 1 and 5; however, there are no clear infrasound detections associated with this activity meaning that extrusion was not accompanied by strong degassing. There are some weakly coherent (~0.5 MCCM) detections in the direction of fissure 8, but nothing similar to what was detected prior to August 5.

Operational aspects

Infrasound had been incorporated in the permanent monitoring network at the USGS Hawaiian Volcano Observatory since 2012 (Thelen and Cooper 2014); however, real-time analysis for monitoring at HVO only started the week before unrest began in 2018. Between 2012 and 2018, much of the standard processing was carried out by the Infrasound Laboratory of the University of Hawai'i at Mānoa (ISLA; https://www.isla.hawaii.edu/), who also operate other infrasound arrays on Island of Hawai'i. Fortuitously, two software packages were installed in late April 2018: iPensive (https://github.com/awech/ipensive) and AVO-alarms (https://github.com/awech/AVO-alarms). Both software packages were developed and in operation at the Alaska Volcano

Observatory (AVO). The iPensive code, based on the methods detailed in Olson and Szuberla (2005) and, similar to our methods in this paper, calculates back-azimuths and displays them in a way that was already familiar in the observatory setting (see Fig. 13B). iPensive displays a mosaic of 10-min analyses in six panels horizontally and as many as 24 panels vertically, giving a duty scientist an easy way of both getting an overview of the activity for a day but also having the ability to zoom into a period of interest. This type of display has wide use across the US volcano observatories to review spectrograms from multiple stations at a given volcano. The AVO-alarms code was used specifically to alarm on a large infrasound signal from a specific range of back-azimuths using the same methods as iPensive. When installed, it was not clear how it would be utilized and it was originally set up with parameters and filters mimicking those used at AVO to detect distant eruptions in the Aleutian Islands including a high-pass filter above 1 Hz.

Alarming for explosion tracking was first setup on station AHUD at a 4-Pa threshold for a source with a back-azimuth from Halema'uma'u ("Halemaumau Airwave AHUD"), but the initial collapse events all had low peak pressures at frequencies greater than 0.5 Hz, and thus, successful alarming on collapse events was inconsistent (Figs. 10 and 18). On May 22, the threshold was lowered to 2.5 Pa to attempt to catch the collapse events. An alarm at station NPT was setup to track infrasonic events from Halema'uma'u as well (named Halemaumau Airwave NPT), but it had inconsistent results because of a bad channel and degrading telemetry in late May as the station was enveloped by the collapse. Observations of the infrasonic waveforms showed that the collapse events were much more energetic below 0.5 Hz and

Fig. 18 Time series of alarm occurrence (colored circles) and collapse events (black vertical lines). The "Halemaumau LP Airwave" alarm began on June 4, the "Halemaumau Airwave AHUD" alarm was operational throughout the eruption, and the "Halemaumau Airwave NPT" was only sporadically operational because of a bad channel and loss of telemetry in late May. Alarm names are used in their original form from the USGS Hawaiian Volcano Observatory

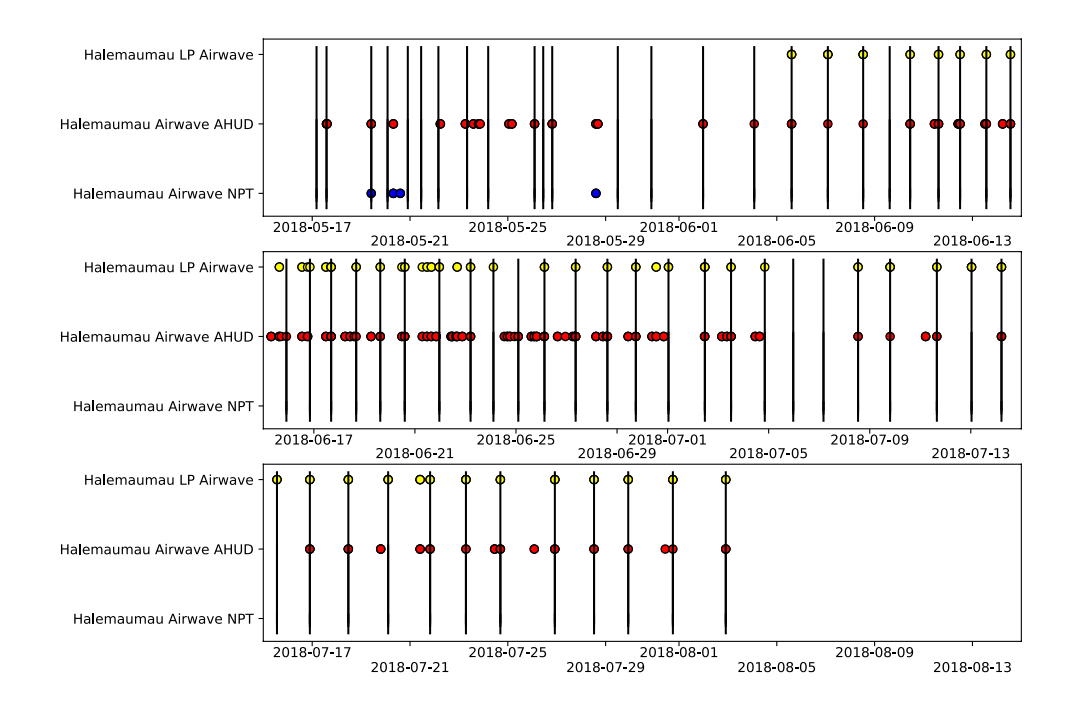




Table 1 Table of performance of the Kīlauea summit alarms. Only the time period that the alarm was active was included in the calculation. Alarms had overlapping time windows so any alarm within three minutes of the collapse event is considered a positive detection

Alarm	Percent alarms associated with collapse	Percent of collapse events detected
Halemaumau LP airwave	81	91
Halemaumau airwave AHUD	31	76
Halemaumau airwave NPT	20	8

an additional alarm was created on June 4, similar to the original AHUD alarm, but using the un-filtered waveform, called the "Halemaumau LP Airwave" alarm. Once implemented, this alarm captured many of the collapse events in real-time, with few alarms occurring outside of collapse events (Fig. 18; Table 1). The alarm became one of the most rapid confirmations of a collapse event especially during times of darkness and/or bad weather when direct observations were unreliable. Comparatively, the "Halemaumau LP Airwave" alarm was better tuned to detect collapse events and only collapse events, but the "Halemaumau Airwave AHUD" alarm was kept in operation in case there were other infrasound processes of interest that needed further analysis (Table 1). Alarming, including infrasound alarming, became reliable enough that it replaced staffing of 24/7 geophysics duty shifts on June 17.

In the LERZ, there was no permanent infrasound in the immediate area prior to the eruption. Subtle topography, dense jungle, and poor cell coverage in certain areas hindered rapid new real-time deployments. Still, infrasound observations were not part of the overall monitoring strategy in the early part of the LERZ eruption. The rationale behind the initial installation of ERZ2 was to enable detection of activity downrift of fissure 17; the installation of infrasound at ERZ2 occurred 11 days after the installation of the seismic site, a period when fissure activation was erratic and short lived. Infrasound could have played an important role during this period of rapidly evolving fissure activity, detecting new breakouts and more efficiently directing ground resources to areas of interest. The AVO-alarms software was established to flag potential fissuring outside of active areas, but after fissure 17, activity never extended farther downrift and an actionable alarm was never triggered. There was also an alarm setup to detect the littoral explosions on the southern coast, but it was never utilized because the risk to people or infrastructure was low.

The addition of the WALE real-time infrasound array produced excellent observations of the fissure 8 activity. Given the long-lived nature of the fissure, the site was well positioned. It also was installed with six elements, providing

more precise back-azimuths and observations, good noise floor characteristics, and redundancy against sensor outages. Further, the offset from the axis of the rift, similar to ERZ2, meant that it would be useful in tracking new breakouts beyond of the bounds of the 2018 activity.

Given the demonstrated utility of infrasound in monitoring during the 2018 eruption, the inclusion of infrasound capability during future responses would be a valuable and cost-effective component of the overall monitoring strategy. Given the ease of deployment with seismic digitizers, infrasound instruments are a useful part of seismic installations. The details of the installation should depend on the goals of the deployment. If interested in tracking fissure initiation, propagation, and demise, an offset installation from the expected eruption site in a downwind direction is ideal. It is also ideal to deploy an array in order to track changes in the location of the source. If, instead, the goal is to track stationary fountaining, then a single sensor, deployed with a seismometer within a couple of kilometers of the eruption site, is likely sufficient. A network of single infrasound sensors may also be used to provide a precise two-dimensional location of the source (Fee et al. 2021) and detail eruptive activity. There are techniques (McKee et al. 2018) that can estimate a back-azimuth from a collocated seismic and infrasound sensor; however, the estimates of back-azimuth are less precise than those obtained with an array of sensors.

Conclusions

Infrasound provided a detailed acoustic record of surficial eruption processes of the 2018 Kīlauea eruption, and we detail several examples where infrasound provided unique insights into the associated processes. For the summit eruption, we characterized the infrasonic and seismic tremor associated with a draining lava lake and described several high-amplitude transient events. Rockfall and explosive events were largely surficial and were marked by seismic and infrasound transients, proto-collapses, and collapse events began after the closing of the conduit and included seismic, infrasound, and tilt transients, along with temporary drops in seismic tremor amplitude. Comparing time-shifted infrasound with seismic records for the first 12 collapse events reveals a collapse mechanism coincident with the seismic very-long-period earthquake. These first 12 collapse events had emissions associated with them, which can be observed in infrasound, while subsequent events have no visually observed emissions but rockfall was observed. The protocollapse and collapse events represent a progression of larger and larger caldera collapses that became repetitive.

During the lower East Rift Zone eruption, infrasound was able to resolve several processes, including



76 Page 22 of 24 Bulletin of Volcanology (2022) 84:76

fountaining and migration of fissuring, explosions from fissures, and explosions from littoral blasts where the lava flow entered the sea. Using arrays of infrasound sensors and incorporating back-azimuths with amplitudes and seismic observations allowed us to better determine the cause of the infrasound. However, our processing approach was adapted to the loudest infrasound source. Future studies with this dataset could apply methods suitable to simultaneously resolve multi-source coherency across all available arrays. More detailed comparison of infrasound with other observations would also help elucidate the associated eruption processes.

Without this dataset, we would know less about the collapse events at the summit of Kīlauea and the fissuring events in the LERZ. Operationally, infrasound proved vital in real-time monitoring. With documentation of these observations and real-time utility, infrasound arrays are an essential part of a real-time monitoring network. The waveform interpretations provided here should support future monitoring of activity associated with caldera collapse, fissure opening, lava lake draining, and effusive activity at basaltic centers in Hawai'i and around the world.

Supplementary information The online version contains supplementary material available at https://doi.org/10.1007/s00445-022-01583-3.

Acknowledgements We wish to acknowledge the USGS staff, as well as partners from other institutions who contributed to the response of the 2018 Kīlauea eruption and provided a wonderfully detailed chronology to correlate different geophysical observations with. In particular, we thank engineers who built and installed the stations that we used in this study. W. T. would like to acknowledge the assistance of Aaron Wech in the installation and configuration of the iPensive and infrasound alarming software. All seismic and infrasonic data used in this paper are available at IRIS. Tilt data are available from https://www.sciencebase.gov/catalog/item/5d8c0330e4b0c4f70d0c339a. Radar data were obtained using the NOAA Weather and Climate Toolkit: https://www.ncdc.noaa.gov/wct. We also thank Leighton Watson, Arthur Jolly, and an anonymous reviewer for their helpful comments.

Funding D. F. received funding from NSF Grant EAR-1901614.

Declarations

Disclaimer Any use of trade, firm, or product names is for descriptive purposes only and does not imply endorsement by the US Government.

References

Anderson KR, Johanson IA, Patrick MR, Gu M, Segall P, Poland MP, Montgomery-Brown EK, Miklius A (2019) Magma reservoir failure and the onset of caldera collapse at Kīlauea Volcano in 2018. Science 366:6470. https://doi.org/10.1126/science.aaz1822



- Bishop JW, Fee D, Szuberla CAL (2020) Improved infrasound array processing with robust estimators. Geophys J Int 221:2058–2074. https://doi.org/10.1093/gij/ggaa110
- Bowman JR, Baker GE, Bahavar M (2005) Ambient infrasound noise. Geophys Res Lett 32(9):L09803. https://doi.org/10.1029/ 2005GL022486
- Caplan-Auerbach J, Duennebier F (2001) Seismic and acoustic signals detected at Lo'ihi Seamount by the Hawai'i Undersea Geo-Observatory. Geochem Geophys Geosyst 2(5):2000GC000113. https://doi.org/10.1029/2000GC000113
- Chouet BA, Dawson PB, James MR, Lane SJ (2010) Seismic source mechanism of degassing bursts at Kīlauea Volcano, Hawaii: results from waveform inversion in the 10–50 s band. J Geophys Res 115(B9):B09311. https://doi.org/10.1029/2009JB006661
- Dawson P, Whilldin D, Chouet B (2004) Application of near real time radial semblance to locate the shallow magmatic conduit at Kīlauea Volcano. Hawaii. Geophys Res Lett 31:21. https://doi.org/ 10.1029/2004GL021163
- De Angelis S, Diaz-Moreno A, Zuccarello L (2019) Recent developments and applications of acoustic infrasound to monitor volcanic emissions. Remote Sensing 11(11):1–18. https://doi.org/10.3390/rs11111302
- den Ouden OFC, Assink JD, Smets PSM, Shani-Kadmiel S, Averbuch G, Evers LG (2020) CLEAN beamforming for the enhanced detection of multiple infrasonic sources. Geophys J Int 221(1):305–317. https://doi.org/10.1093/gji/ggaa010
- Fee D, Garcés M (2007) Infrasonic tremor in the diffraction zone. Geophys Res Lett 34:16. https://doi.org/10.1029/2007GL030616
- Fee D, Matoza RS (2013) An overview of volcano infrasound: from hawaiian to plinian, local to global. J Volcanology Geothermal Res 249(3):123–139. https://doi.org/10.1016/j.jvolgeores.2012. 09.002
- Fee D, Garcés M, Patrick M, Chouet B, Dawson P, Swanson D (2010) Infrasonic harmonic tremor and degassing bursts from Halema'uma'u Crater, Kīlauea Volcano. Hawaii J Geophys Res 115(B11):B11316. https://doi.org/10.1029/2010JB007642
- Fee D, Toney L, Kim K, Sanderson RW, Iezzi AM, Matoza RS, De Angelis S, Jolly A, Lyons J, Haney M (2021) Local explosion detection and infrasound localization by reverse time migration using 3-D finite-difference wave propagation. Front Earth Sci 9:44. https://doi.org/10.3389/feart.2021.620813
- Fee D, Garces M, Orr T, Poland M (2011) Infrasound from the 2007 fissure eruptions of Kīlauea Volcano, Hawai'i. https://doi.org/10. 1029/2010GL046422
- Fee D, Lyons JJ, Thelen WA, Shiro B, Anderson KR, Waite GP, Chang JC (2018) Infrasound from the repeated collapses of Kīlauea caldera: high-resolution source location and waveform inversion. AGU Fall Meeting V41B-04. https://agu.confex.com/agu/fm18/meetingapp.cgi/Paper/440456. Accessed 16 March 2022
- Gansecki C, Lee RL, Shea T, Lundblad SP, Hon K, Parcheta C (2019) The tangled tale of Kīlauea's 2018 eruption as told by geochemical monitoring. Science 366(6470):eaaz0147. https://doi.org/10.1126/science.aaz0147
- Garcés M, Harris A, Hetzer C, Johnson J, Rowland S, Marchetti E, Okubo P (2003) Infrasonic tremor observed at Kīlauea Volcano. Hawai'i. Geophys Res Lett 30:20. https://doi.org/10.1029/2003g 1018038
- Garcés M, Thelen WA (2015) Infrasound monitoring in Hawaii, near surface Asia-Pacific conference. Waikoloa, 7–10
- Garcia MO, Rhodes JM, Wolfe EW, Ulrich GE, Ho RA (1992) Petrology of lavas from episodes 2-47 of the Puu Oo eruption of Kilauea Volcano, Hawaii: Evaluation of magmatic processes. Bull Volcanol 55(1-2):1-16. https://doi.org/10.1007/BF00301115



Bulletin of Volcanology (2022) 84:76 Page 23 of 24 76

Gestrich JE, Fee D, Matoza RS, Lyons JJ, Ruiz MC (2021) Fitting jet noise similarity spectra to volcano infrasound data. Earth Space Sci 8:11. https://doi.org/10.1029/2021EA001894

- Goldstein P, Archuleta RJ (1987) Array analysis of seismic signals. Geophys Res Lett 14(1):13–16. https://doi.org/10.1029/GL014 i001p00013
- Haney MM, Van Eaton AR, Lyons AR, Kramer JJ, Fee RLD, Iezzi AM (2018) Volcanic thunder from explosive eruptions at Bogoslof Volcano. Alaska Geophys Res Lett 45(8):3429–3435. https://doi. org/10.1002/2017GL076911
- Heliker C, Mattox T (2003) The First Two Decades of the Pu'u'o'o-Kupaianaha eruption: chronology and selected bibliography. US Geol Surv Prof Pap 1676:1–28. https://doi.org/10.3133/pp1676
- Iezzi AM, Matoza RS, Bishop JW, Bhetanabhotla S, Fee D (2022) Narrow-band least-squares infrasound array processing. Seismolog Res Lett. https://doi.org/10.1785/0220220042
- Johanson IA, Miklius A (2019) Tiltmeter data from Kīlauea Volcano, Hawaii, spanning the 2018 eruption and earthquake sequence: U.S. Geological Survey data release. https://doi.org/10.5066/ P9310M9N
- Johnson JB, Ripepe M (2011) Volcano infrasound: a review. J Volcanol Geoth Res 206(3–4):61–69. https://doi.org/10.1016/j.jvolgeores. 2011.06.006
- Johnson JB, Ruiz MC, Ortiz HD, Watson LM, Viracucha G, Ramon P, Almeida M (2018) Infrasound Tornillos produced by Volcán Cotopaxi's deep crater. Geophys Res Lett 45(11):5436–5444. https://doi.org/10.1029/2018GL077766
- Johnson JB, Watson LM, Palma JL, Dunham EM, Anderson JF (2018) Forecasting the eruption of an open-vent volcano using resonant infrasound tones. Geophys Res Lett 45(5):2213–2220. https://doi. org/10.1002/2017GL076506
- Jolly A, Lokmer I, Christenson B, Thun J (2018) Relating gas ascent to eruption triggering for the April 27, 2016, White Island Whakaari, New Zealand eruption sequence. Earth, Planets and Space 70:1. https://doi.org/10.1186/s40623-018-0948-8
- Klein FW, Koyanagi R, Nakata J, Tanigawa W (1987) The seismicity of Kilaueas's magma system. In R. W. Decker, T. L. Wright, & P. H. Stauffer (Eds.), Volcanism in Hawaii: USGS professional paper 1350(43):1019–1185
- le Pichon A, Maurer V, Raymond D, Hyvernaud O (2004) Infrasound from ocean waves observed in Tahiti. Geophys Res Lett 31:19. https://doi.org/10.1029/2004GL020676
- Lyons JJ, Haney MM Fee D, Paskievitch JF (2014) Distinguishing high surf from volcanic long-period earthquakes. Geophys Res Lett 41. https://doi.org/10.1002/2013GL058954
- Lyons JJ, Dietterich HR, Patrick MR, Fee D (2021) High-speed lava flow infrasound from Kīlauea's fissure 8 and its utility in monitoring effusion rate. Bull Volcanol 83(66). https://doi.org/10.1007/s00445-021-01488-7
- Marcillo O, Johnson JB (2010) Tracking near-surface atmospheric conditions using an infrasound network. J Acoustical Soc America 128(1):EL14–EL19. https://doi.org/10.1121/1.3442725
- Marcillo O, Johnson JB, Hart D (2012) Implementation, characterization, and evaluation of an inexpensive low-power low-noise infrasound sensor based on a micromachined differential pressure transducer and a mechanical filter. J Atmos Oceanic Tech 29(9):1275–1284. https://doi.org/10.1175/JTECH-D-11-00101.1
- Matoza RS, Fee D, Garcés MA (2010) Infrasonic tremor wavefield of the Pu`u`Ō`ō crater complex and lava tube system, Hawaii, in April 2007. J Geophys Res 115(B12):B12312. https://doi.org/10.1029/2009JB007192
- McKee K, Fee D, Haney M, Matoza RS, Lyons J (2018) Infrasound signal detection and back azimuth estimation using ground-coupled airwaves on a seismo-acoustic sensor pair. J Geophys Res: Solid Earth 123(8):6826–6844. https://doi.org/10.1029/2017JB015132

- Minakami T (1974) Seismology of volcanoes in Japan. Develop Solid Earth Geophys 6:1–27. https://doi.org/10.1016/b978-0-444-41141-9.50007-3
- Neal CA, Brantley SR, Antolik L, Babb JL et al (2019) The 2018 rift eruption and summit collapse of Kīlauea Volcano. Science 363(6425):367–374. https://doi.org/10.1126/science.aav7046
- Olson JV, Szuberla CAL (2005) Distribution of wave packet sizes in microbarom wave trains observed in Alaska. J Acoustical Society America 117(3):1032–1037. https://doi.org/10.1121/1.1854651
- Orr TR, Thelen WA, Patrick MR, Swanson DA, Wilson DC (2012) Explosive eruptions triggered by rockfalls at Kīlauea volcano. Hawai'i Geology 41(2):207–210. https://doi.org/10.1130/ G33564.1
- Patrick M, Wilson D, Fee D, Orr T, Swanson D (2011) Shallow degassing events as a trigger for very-long-period seismicity at Kīlauea Volcano, Hawai'i. Bull Volcanol 73(9):1179–1186. https://doi.org/10.1007/s00445-011-0475-y
- Patrick M, Dietterich HJL, Diefenbach A, Parcheta C, Anderson K, Namiki A, Sumita I, Kauahikaua J (2019) Cyclic lava effusion during the 2018 eruption of Kīlauea Volcano. Science 366:10. https://doi.org/10.1126/science.aay9070
- Patrick M, Orr T, Anderson K, Swanson D (2019) Eruptions in sync: improved constraints on Kīlauea Volcano's hydraulic connection. Earth Planet Sci Lett 507:50–61. https://doi.org/10.1016/J.EPSL. 2018.11.030
- Patrick MR, Orr T, Sutton AJ, Lev E, Thelen WA, Fee D (2016) Shallowly driven fluctuations in lava lake outgassing (gas pistoning), Kīlauea Volcano. Earth Planet Sci Lett 433. https://doi.org/10.1016/j.epsl.2015.10.052
- Patrick MR, Orr T, Swanson D, Houghton B, Wooten K, Desmither L, Parcheta C, Fee D (2021) Kīlauea's 2008–2018 summit lava lake—chronology and eruption insights. In: Patrick M, Orr T Swanson D, Houghton B (eds) The 2008–2018 summit lava lake at Kīlauea Volcano, Hawai'i: U.S. Geological Survey Professional Paper 1867 50. https://doi.org/10.3133/pp1867A
- Perret FA (1950) Volcanological observations. Publ, Carnegie Inst. Wash
- Poland MP, Montgomery-Brown AEK (2014) Magma supply, storage, and transport at shield stage Hawaiian Volcanoes. US Geol SurvProfessional Paper 1801(2010):1–52. https://doi.org/10.3133/pp1801
- Poland MP, Carbone D, Patrick MR (2021) Onset and evolution of Kīlauea's 2018 flank eruption and summit collapse from continuous gravity. Earth Planet Sci Lett 117003:567. https://doi.org/10.1016/j.epsl.2021.117003
- Poland MP, Miklius A, Johanson IA, Anderson KR (2021b) A decade of geodetic change at Kīlauea's summit-observations, interpretations, and unanswered questions from studies of the 2008–2018 Halema'uma'u Eruption. In: Patrick M, Orr T, Swanson D, Houghton B (eds) The 2008–2018 summit lava lake at Kīlauea Volcano, Hawai'i: U.S. Geological Survey Professional Paper 1867. pp 1–29. https://doi.org/10.3133/pp1867G
- Ripepe M, Marchetti E (2002) Array tracking of infrasonic sources at Stromboli volcano. Res Lett 29(22):2076. https://doi.org/10.1029/2002GL015452
- Rost S, Thomas C (2002) Array seismology: methods and applications. Rev Geophys 40(3):1008
- Ryan MP (1988) The mechanics and three-dimensional internal structure of active magmatic systems: Kīlauea volcano. Hawaii J Geophys Res 93(B5):4213–4248
- Shelly DR, Thelen WA (2019) Anatomy of a caldera collapse Kīlauea summit seismicity sequence in high resolution. Geophys Res Lett 2014:2019GL085636. https://doi.org/10.1029/2019GL085636
- Shiro BR, Zoeller MH, Kamibayashi K, Johanson IA, Parcheta C, Patrick MR, Nadeau P, Lee L, Miklius A (2021) Monitoring network



76 Page 24 of 24 Bulletin of Volcanology (2022) 84:76

changes during the 2018 Kīlauea Volcano eruption. Seismol Res Lett 92(1):102–118. https://doi.org/10.1785/0220200284

- Staudacher T, Ferrazzini V, Peltier A, Kowalski P, Boissier P, Catherine P, Lauret F, Massin F (2009) The April 2007 eruption and the Dolomieu crater collapse, two major events at Piton de la Fournaise (La Réunion Island, Indian Ocean). J Volcanol Geoth Res 184(1–2):126–137. https://doi.org/10.1016/j.jvolgeores.2008. 11.005
- Swanson D, Duffield WA, Fiske RS (1976) Displacement of the south flank of Kīlauea Volcano: the result of forceful intrusion of magma into rift zones. U.S Geol Surv Prof Pap 963:39
- Tepp G, Hotovec-Ellis A, Shiro B, Johanson I, Thelen W, Haney MM (2020) Seismic and geodetic progression of the 2018 summit caldera collapse of Kīlauea volcano. Earth Planet Sci Lett 540:116250. https://doi.org/10.1016/j.epsl.2020.116250
- Thelen WA, Cooper J (2014) An analysis of three new infrasound arrays around Kīlauea Volcano. U.S. Geological Survey Open-File Report 2014–1253, 29 https://doi.org/10.3133/ofr20141253
- Tilling R, Dvorak J (1993) Anatomy of a basaltic volcano. Nature 363:125–133

- Ulivieri G, Ripepe M, Marchetti E (2013) Infrasound reveals transition to oscillatory discharge regime during lava fountaining: Implication for early warning. Geophys Res Lett 40(12):3008–3013. https://doi.org/10.1002/grl.50592
- USGS Hawaiian Volcano Observatory (HVO) (1956) Hawaiian Volcano Observatory Network. International Federation of Digital Seismograph Networks. https://doi.org/10.7914/SN/HV
- Wessel PL, Uieda JF, Scharroo L, Wobbe R, Smith F, Tian D (2019) The Generic Mapping Tools version 6. Geochem Geophys Geosyst 20:5556–5564. https://doi.org/10.1029/2019GC008515
- Wolfe E, Garcia M, Jackson D, Koyanagi R, Neal C, Okamura A (1987) The Puu oo eruption of Kilauea Volcano, episodes 1–20, January 3 1983, to June 8, 1984. In: Volcanism in Hawaii. U.S. Geological Survey Professional Paper 1350, pp 471–508
- Wright, TL Klein, F. (2014). Two hundred years of magma transport and storage at Kilauea Volcano, Hawai'i, 1790–2008. U.S. Geological Survey Professional Paper 1806, 240pp.

